Computers and Structures 257 (2021) 106647

Contents lists available at ScienceDirect

Computers and Structures

journal homepage: www.elsevier.com/locate/compstruc

Assessing the safety of vaulted masonry structures using thrust network analysis

R. Maia Avelino *, A. Iannuzzo, T. Van Mele, P. Block

ETH Zürich, Institute of Technology in Architecture (ITA), Block Research Group (BRG), Stefano-Franscini-Platz 1, HIB E 45, 8093 Zürich, Switzerland

ARTICLE INFO

Article history:
Received 3 March 2021
Accepted 22 July 2021

Keywords:
Masonry assessment
Thrust network analysis
Optimisation
Equilibrium analysis
Limit analysis
Geometric safety factor

ABSTRACT

This paper presents a methodology to assess the stability of vaulted masonry structures using Thrust Network Analysis (TNA). It offers a new numerical strategy to compute the Geometric Safety Factor (GSF) of a given structure by directly evaluating its minimum thickness. Moreover, it provides an approach for tracing the vault's stability domain based on its extreme thrust values, which indicates the robustness of the structure. Together, these outcomes represent a proper measure of the safety level of masonry structures. Such results are obtained from constrained nonlinear optimisation problems (NLPs) with appropriate objective functions and constraints enforcing the limit analysis' admissibility criteria. Networks with fixed horizontal projection are considered, for which the spatial geometry is a function of the independent force densities and the height of the support vertices. A faster, interactive procedure is proposed to improve the selection of such independent force densities. The range of applications of the present method includes arbitrary network topologies and different support conditions. Beyond analytically described geometries, the method can deal with geometries obtained numerically (e.g. from point clouds). The presented strategy is implemented in a Python-based package, and relevant applications illustrate the method's potential in assessing the stability of three-dimensional historic vaulted structures.

1. Introduction

The assessment of three-dimensional unreinforced masonry (URM) structures is a complex subject in structural engineering that demands specific analysis tools and methods to provide adequate output about the safety of an existing structure. Currently, such specialised methods and tools are not widely available [1].

The collapse of masonry structures occurs due to a lack of stability rather than insufficient material strength [2,3]. For this reason, the application of Equilibrium Methods based on Limit Analysis constitutes a valid method to assess masonry structures.

Heyman's three material assumptions [4] provide a rigorous framework for applying Limit Analysis to masonry structures [2,5]. According to the *safe theorem* of limit analysis, a structure is safe if an admissible internal stress state can be found. As a consequence of Heyman's assumptions, admissible stress states must be compressive and contained within the structural envelope.

Equilibrium methods model the internal forces in the structure and allow for identifying these admissible stress states. Among its advantages, limit analysis equilibrium methods can be applied even if detailed information about material properties and stereotomy are unknown. Moreover, the application of the safe theorem guarantees that the solution is conservative, i.e., that it corresponds to a lower-bound estimation of the collapse state.

The search for admissible stress states has been extensively and historically applied for arches using the *thrust line* method [2,5,6] and has been extended to axisymmetric structures such as sliced domes [7–9] and spiral stairs [10]. However, extending equilibrium methods to general three-dimensional structures is challenging because of their intrinsic high indeterminacy. In recent years, various lower-bound equilibrium formulations have been developed to cope with the assessment of three-dimensional masonry structures. These strategies can be divided in two groups: *thrust surface* and *thrust network* approaches.

The first group, thrust surface approaches, represents the internal forces in the masonry as a continuous membrane having the forces computed through the use of the Airy Stress Functions (ASF). Initially proposed in [11] and further developed in [12–15], the method approximates the continuum surfaces in a regular polyhedral domain. In [16], NURBS are used to describe the surfaces, and in [17,18], triangular and quad meshes are considered. Using this approach, the magnitude of the membrane forces are

* Corresponding author.
E-mail addresses: maia@arch.ethz.ch (R. Maia Avelino), iannuzzo@arch.ethz.ch (A. Iannuzzo), van.mele@arch.ethz.ch (T. Van Mele), block@arch.ethz.ch (P. Block).

https://doi.org/10.1016/j.compstruc.2021.106647
0045-7949/

taken from the curvature of the ASF, and the vertical equilibrium is computed with differential equations. Thus, an admissible stress state can be identified by verifying that the membrane is contained within the geometric bounds of the masonry (intrados and extrados) and that the ASF is concave (compression-only).

The present paper focuses on the second group, thrust network approaches, in which the internal stress states are represented by a discrete network of forces. This methodology was proposed in [19,20] as Thrust Network Analysis (TNA). TNA has been applied in combination with optimisation algorithms [21,22], and it is recognised as a flexible and suitable method for a wide range of assessment scenarios, i.e., dealing with diverse sets of supports and discontinuities. In TNA, the stresses are considered as normal forces along the edges, and external forces are applied to the vertices of the network. By restricting the loading case to vertically applied forces, the vertical and horizontal equilibria can be decoupled [19]. In this method, distinct treatments to the horizontal equilibria are possible. In its original formulation [20], the horizontal equilibrium is computed by using a reciprocal graph to represent the magnitude and equilibrium of the internal forces. In an ensuing publication [23], this indeterminacy is tackled by defining the forces in the independent edges that form a basis of the forces needed to describe the space of horizontally equilibrated solutions. The latter has influenced recent studies [24], in which a constrained nonlinear optimisation problem was used to find states of minimum and maximum (horizontal) thrusts. With TNA, an admissible stress state corresponds to a thrust network with compressive normal forces contained within the envelope of the structure.

However, even with the advances in the literature to date, determining the level of stability or closeness to collapse of masonry structures with lower-bound equilibrium methods is not straightforward. Indeed, finding only one admissible stress state is sufficient to guarantee that the structure is safe in its configuration, but it does not give any additional information about the level of stability, which is a crucial requirement for an overall stability assessment. The level of stability can be assessed through the Geometric Safety Factor (GSF) [25], which has been achieved for simple shapes in previous research using different strategies: by minimising the vertical distance to the middle surface in [23,22,26], by linearly decreasing the structural section in [27,20], and by successively generating geometries with reduced thicknesses until admissible solutions can no longer be computed [28,29]. However, the first two strategies do not consider a proper orthogonal reduction of the structural thickness, while the third strategy requires the definition (or creation) of multiple geometries and the solution of the corresponding mechanical problems.

This paper introduces a novel strategy to directly compute the structure's GSF as a result of a constrained nonlinear optimisation problem (NLP) by directly minimising the structural thickness subjected to the limit analysis' admissibility criteria. This formulation can be applied to masonry structures of any shape and cope with cases in which the structural geometry is defined by analytical expressions, or when only an approximated (non-analytic) geometry is available, e.g., from surveying point clouds.

Nonetheless, the GSF alone is not sufficient to provide a complete description of the structural robustness. Additional information can be obtained from the ratio among the maximum and minimum (horizontal) thrusts exerted by the structure [30,31,28], which relates to the size of the admissible stress states. Therefore, besides providing a direct optimisation to compute the GSF, this paper develops a procedure to trace the structure's stability domain until the collapse state. This domain is defined through the extremes of maximum and minimum (horizontal) thrusts for decreasing structural thicknesses (i.e., until its limit thickness). Its area represents a proper measurement of the space of admissible stress states and together with the GSF it offers a proper assessment strategy that can be applied to general geometries with minimal input information.

The strategy presented in this paper is implemented in a Python-based tool within the COMPAS open-source framework [32]. The numerical optimisations are solved with Sequential Least Squares Programming (SLSQP) techniques [33], using an analytical description for the gradients and computing the equilibrium with independent edges as in [23].

The organisation of the paper is as follows: Section 2 presents the limit analysis theoretical background; Section 3 formalises the numerical procedure to obtain thrust networks with different spatial distributions; Section 4 introduces the different optimisation problems used to determine the structure's GSF and to trace the stability domain; Section 5 shows applications of the present methodology to the assessment of distinct vaulted masonry structures, including domes (5.1), square cross vaults (5.2), and a case study obtained from a point cloud (5.3) based on the central nave cross vault of the Amiens Cathedral. Finally, Section 6 summarises the results obtained and points to future work.

2. Theoretical background

The main aspects of the limit analysis applied to masonry structures are described in this section. The lower-bound limit analysis is described in Section 2.1. Following, the concepts of limit state and stability domain are formalised in 2.2. Then, the specific thrust networks needed to perform the assessment are defined in 2.3.

2.1. Lower-bound limit analysis of masonry structures

Limit Analysis focuses on the collapse states of the structure rather than computing its current stress state [34]. Heyman [4] shows that limit analysis holds for URM structures under three assumptions:

(i) masonry's compressive strength is infinite,
(ii) masonry's tensile strength is considered null, and
(iii) no sliding occurs between the elements of the structure.

These assumptions, even if crude, accurately model masonry structures, because: (i) the levels of stress encountered are usually low and far from the material's compressive strength; (ii) the tensile strength of the material is two orders of magnitude less than its compressive strength, while the mortar connecting the blocks is usually weak or decayed; and (iii) existing historic URM structures, in general, were built carefully with appropriate stereotomy or construction details to avoid sliding failure.

Within the limit analysis theory, the static and kinematic theorems can be used to provide information about the collapse of the structure. The former, also known as the safe theorem, states that if any admissible stress field is found for a given structure, then the structure is safe under the applied loads, and the solution corresponds to a lower-bound of the collapse state. The latter, also known as the unsafe theorem, states that once a kinematically admissible mechanism is found, the structure is unsafe under the applied loads, and the solution corresponds to an upper-bound of the collapse state [35–38].

This paper focuses on the safe theorem. The stress states are represented by a thrust network (TN), where axial forces are considered in the edges, and the external loads are applied in the vertices of the network. From these assumptions, an admissible stress state corresponds to a compressive TN entirely contained within the envelope of the structure [4,2]. The numerical procedure to find such equilibrium states will be described in Section 3.

A few known cases have been documented in the literature in which Heyman's assumptions don't hold, or can be relaxed. The reader is referred to [39,40] for a discussion on failure modes considering sliding, which can not be taken into account with the present methodology as no specific stereotomy is considered. Additionally, in [41–43] the appearance of tensile resistance due to friction in the joints of masonry is discussed, which is especially significant for specific stereotomies. In the present formulation, tensile forces could also be taken into account by relaxing the compression-only requirement, however, this publication holds to the compression-only assumption (ii) across all edges of the network.

2.2. Limit state and stability domain

Finding one admissible stress state informs if the structure in its configuration is safe or not, but it does not provide information about the level of stability. Assessing the level of stability implies answering how far the structure is from the collapse state, and how stable it is in its current configuration. The first question can be answered through the evaluation of the GSF, while the second demands an evaluation of the stability domain. In the next subsections, a theoretical overview of these concepts is provided.

2.2.1. Limit state

Heyman [4] defines the GSF as the ratio among the current structural thickness (t) and the minimum thickness ($t_{\min}$) of the tightened cross-section, which still contains an admissible stress state. A minimal thickness structure is said to be at its limit state, as only one admissible stress state is possible, i.e., the corresponding domain of admissible stress states reduces to a singleton [13]. Therefore, the GSF represents a measure of how far the structure is from its limit or collapse state.

Similar reasoning can be used to describe the collapse state corresponding to external incremental loads, described by the so-called collapse multiplier [5]. Dealing with incremental loads is also possible with the present methodology; however, we limit the scope of the present paper to the case of self-weight only.

2.2.2. Stability domain

The stability domain of a given masonry structure is the set of all admissible stress states. A reasonable measure of this domain is represented by its extreme (minimum and maximum) thrusts. Instances of such representation are present in the literature [30,29]. For all but the limit state, the minimum and maximum thrust will correspond to different stress states and have distinct horizontal thrust values. However, at the limit state minimum and maximum thrust coincide.

Thus, this work traces the stability domain for reduced values of thickness, until the collapse state (i.e., when the thickness is minimum). Understanding how the stability domain changes as a function of the thickness gives a direct measure of the robustness of the structure from its initial state, until the collapse state. This robustness can be associated with the structure's capacity to carry additional imposed loads or undergo external settlements.

Therefore, the stability domain of the structure in its configuration together with the evaluation of the GSF represents a proper measure of the safety level.

2.3. Specific thrust networks

To investigate the structure's limit state and stability domain, three specific thrust networks are defined:

- **Minimum Thickness Network:** the thrust network corresponding to the minimum thickness. In this paper, the geometrical description is based on the middle surface of the structure with the thickness applied orthogonally to it. The well-known minimum thickness problem of an arch is illustrated in Fig. 1a.
- **Minimum Thrust Network:** the thrust network resulting in the minimum horizontal thrust exerted on the supports. For a 2D arch, this solution is the deepest possible thrust line solution in the structure (Fig. 1b).
- **Maximum Thrust Network:** the thrust network associated with the maximum horizontal thrust exerted on the supports. For 2D arches, the maximum thrust state corresponds to the shallowest possible thrust line solution in the structure (Fig. 1c).

The GSF can be directly obtained by solving the minimum thickness problem (Section 2.2.1) while finding the limits of (minimum and maximum) thrusts for a given envelope allows tracing the stability domain (Section 2.2.2).

A known connection with kinematics exists for these states [2], the minimum thrust forms when an outward displacement is imposed to the structure (passive state), and the maximum thrust when an inwards displacement is imposed (active state).

The following sections will cover the numerical procedure required to find such specific thrust networks as solutions to NLPs.

3. Numerical implementation

This Section presents the numerical implementation to compute admissible TNs. In Section 3.1, the equilibrium equations in networks are expressed in matrix form. In Section 3.2, TNs with fixed horizontal projection are introduced and the equilibrium equations are rewritten as a function of the independent force densities, as in [23]. Section 3.3 presents a fast numerical method to select independent edges. In Section 3.4, the limit analysis' admissibility constraints are formulated numerically.

3.1. General equilibrium of networks

A network composed of n vertices, in which n_i are internal and n_b are support vertices, connected by m edges is considered. The

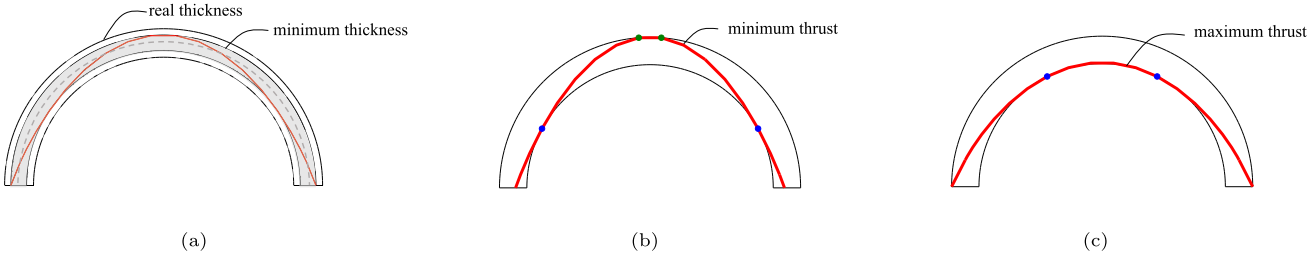

Fig. 1. Illustration of the objective function for an arch discretised with 20 blocks: (a) minimum, and real thickness allowing computation of the GSF; (b) minimum thrust with the deepest thrust line; (c) maximum thrust with the shallowest thrust line.

topology of the network is represented by the connectivity matrix $\mathbf{C}$ $[m \times n]$ [44], which is sliced in the submatrices $\mathbf{C}_\mathrm{i}$ $[m \times n_\mathrm{i}]$ and $\mathbf{C}_\mathrm{b}$ $[m \times n_\mathrm{b}]$, corresponding to the internal and support vertices. Let $\mathbf{x}, \mathbf{y}, \mathbf{z}$ be the vertex coordinates of the network, $\mathbf{p}_\mathrm{x}, \mathbf{p}_\mathrm{y}, \mathbf{p}_\mathrm{z}$ the n_i-dimensional vectors representing the forces applied on the internal vertices, and $\mathbf{q}$ the force density vector whose i-th component q_i is the ratio between the edge's force f_i and length l_i. By introducing the coordinate differences matrices $\mathbf{U} = \mathrm{diag}(\mathbf{Cx}), \mathbf{V} = \mathrm{diag}(\mathbf{Cy})$, and $\mathbf{W} = \mathrm{diag}(\mathbf{Cz})$ $[m \times m]$ storing the Cartesian lengths of each edge, the $3n_\mathrm{i}$ equilibrium equations of the network vertices can be written as:

$$\mathbf{C}_\mathrm{i}^\mathrm{T}\mathbf{U}\mathbf{q} = \mathbf{p}_\mathrm{x}, \tag{1a}$$

$$\mathbf{C}_\mathrm{i}^\mathrm{T}\mathbf{V}\mathbf{q} = \mathbf{p}_\mathrm{y}, \tag{1b}$$

$$\mathbf{C}_\mathrm{i}^\mathrm{T}\mathbf{W}\mathbf{q} = \mathbf{p}_\mathrm{z}. \tag{1c}$$

The equilibrium summarised by Eqs. (1) describes a spatial TN (defined through its vertices position) as a function of the edge force densities $\mathbf{q}$. In Section 3.2 the particular case in which the horizontal projection of the network is fixed is described.

3.2. Thrust networks with fixed horizontal projection

In the present work, two key assumptions are made. The first assumption imposes that the horizontal projection of the network, called *form diagram* [19] is fixed. The second assumption is that only gravity loads ($\mathbf{p}_\mathrm{z}$) are considered, which are calculated after projecting each vertex to the middle surface of the structure and computing its tributary area. As a result, the horizontal and vertical equilibria can be decoupled, and 1a and 1b can be combined and rewritten as:

$$\begin{bmatrix} \mathbf{C}_\mathrm{i}^\mathrm{T}\mathbf{U} \\ \mathbf{C}_\mathrm{i}^\mathrm{T}\mathbf{V} \end{bmatrix} \mathbf{q} = \mathbf{E}\mathbf{q} = \mathbf{0}, \tag{2}$$

where $\mathbf{E}$ $[2n_\mathrm{i} \times m]$ is the (horizontal) equilibrium matrix, which is known for a network with fixed horizontal projection.

Let $\mathbf{Q} = \mathrm{diag}(\mathbf{q})$ $[m \times m]$ be the diagonal matrix of force densities, then the vertical equilibrium equation (Eq. (1c)) can be rewritten such that the height of the internal vertices $\mathbf{z}_\mathrm{i}$ can be computed as a function of force densities $\mathbf{q}$ and support heights $\mathbf{z}_\mathrm{b}$:

$$\mathbf{z}_\mathrm{i} = (\mathbf{C}_\mathrm{i}^\mathrm{T}\mathbf{Q}\mathbf{C}_\mathrm{i})^{-1}(\mathbf{p}_\mathrm{z} - (\mathbf{C}_\mathrm{i}^\mathrm{T}\mathbf{Q}\mathbf{C}_\mathrm{b})\mathbf{z}_\mathrm{b}), \tag{3}$$

where, for the convenience of computing compression-only TNs, the convention adopted here assumes compression forces and gravity loads as positive, as in [23].

Vectors $\mathbf{R}_\mathrm{x}, \mathbf{R}_\mathrm{y}$, and $\mathbf{R}_\mathrm{z}$ $[n_\mathrm{b} \times 1]$ store the magnitude x-, y-, z-components of the thrust exerted on the supports. Since no horizontal loads are considered, they can be expressed as follows:

$$\mathbf{R}_\mathrm{x} = \mathbf{C}_\mathrm{b}^\mathrm{T}\mathbf{U}\mathbf{q}, \tag{4a}$$

$$\mathbf{R}_\mathrm{y} = \mathbf{C}_\mathrm{b}^\mathrm{T}\mathbf{V}\mathbf{q}, \tag{4b}$$

$$\mathbf{R}_\mathrm{z} = \mathbf{C}_\mathrm{b}^\mathrm{T}\mathbf{W}\mathbf{q} - \mathbf{p}_{\mathrm{z,b}}, \tag{4c}$$

where $\mathbf{p}_{\mathrm{z,b}}$ $[n_\mathrm{b} \times 1]$ represents the share of the self-weight (i.e., tributary area) which is lumped to the support vertices.

To keep the projection fixed, i.e., to guarantee that Eq. (2) holds, Block et al. [23] introduced the independent force densities $\mathbf{q}_\mathrm{ind}$. They correspond to a base (k independent columns) of the nullspace of the equilibrium matrix $\mathbf{E}$. Let $\mathbf{q}_\mathrm{dep}$ and $\mathbf{q}_\mathrm{ind}$ be the force densities associated with the dependent and independent edges, respectively. By slicing the equilibrium matrix $\mathbf{E}$ into two submatrices, $\mathbf{E}_\mathrm{dep}$ $[2n_\mathrm{i} \times (m-k)]$ and $\mathbf{E}_\mathrm{ind}$ $[2n_\mathrm{i} \times k]$, corresponding to the $(m-k)$ dependent and k independent edges the horizontal equilibrium can be written as follows:

$$\mathbf{q}_\mathrm{dep} = -\mathbf{E}_\mathrm{dep}^\dagger \mathbf{E}_\mathrm{ind}\mathbf{q}_\mathrm{ind}, \tag{5}$$

with $\mathbf{E}_\mathrm{dep}^\dagger$ as the generalised inverse or Moore-Penrose pseudo-inverse of $\mathbf{E}_\mathrm{dep}$. Eq. (5) describes the relation between $\mathbf{q}_\mathrm{dep}$ and $\mathbf{q}_\mathrm{ind}$ through a linear map using the sliced $\mathbf{E}$ matrices. In this sense, for a given $\mathbf{q}_\mathrm{ind}$, $\mathbf{q}_\mathrm{dep}$ can be directly computed solving the horizontal equilibrium and keeping the horizontal projection of the network unchanged. A method to find the nullspace of $\mathbf{E}$, i.e., determine the independent edges, is presented in Section 3.3.

3.3. Finding independent edges

The independent force densities $\mathbf{q}_\mathrm{ind}$ correspond to the basis of the nullspace of the equilibrium matrix $\mathbf{E}$ [45,46]. Multiple different sets of edges can be chosen to span the null space of $\mathbf{E}$ [47].

Previous works [23,45,24] applied a Gauss-Jordan Elimination (GJE) to find the reduced row-echelon form (RREF) of $\mathbf{E}$. However, this method is known to be imprecise, especially for ill-conditioned matrices, and time-consuming for large $\mathbf{E}$. This work proposes an interactive method, as in [48], based on Singular Value Decomposition (SVD) which is more robust and less time-consuming.

In this interactive method, the matrix $\mathbf{E}$ is reconstructed column by column. Each time a column is added, the matrix rank is checked through SVD. After such addition, if the rank of the matrix is not increased, then the column belongs to the nullspace of $\mathbf{E}$, and the corresponding edge can be taken as an independent.

Finding the independent edges for large networks was the bottleneck in terms of time consumption in previous studies [23]. Therefore, refining this process improved the computational pipeline, and will be used for the formulation of the optimisation in Section 4.

3.4. Admissible thrust networks

Following the assumptions of 2.1, admissible stress states are defined numerically in this Section. An admissible stress state is represented by thrust networks of purely compressive forces lying within the structural geometry. The compression-only requirement is enforced constraining the force densities to be positive, i.e., imposing a non-negative $\mathbf{q}$component-wise. As it is not guaranteed that a positive $\mathbf{q}_\mathrm{ind}$ will result in a positive $\mathbf{q}$ (Eq. (5)), the compression-only requirement has to be enforced for all edges.

The geometric admissibility criterion is enforced in the vertices of the thrust network, constrained to lie within the structural thickness. Specifically, the elevation z_i of each vertex i is constrained to lie between intrados (z_i^LB) and extrados (z_i^UB). Fig. 2 illustrates these constraints geometrically.

A special treatment is given to the support vertices. As for the internal vertices, the height z_j of each support vertex j must also be constrained between intrados (z_j^LB) and extrados (z_j^UB). However, in some cases, as illustrated by the dome in Fig. 2, the projection of the supports on the intrados may not exist. Whenever such a condition occurs, a positive parameter z_min is assumed as illustrated in Fig. 2.

Additionally, to guarantee the geometric admissibility criterion, another constraint has to be imposed: the thrust exerted on the supports must not cross the vault geometry. With respect to the support j, this can be achieved by requiring that the thrust $\mathbf{R}_j$ is contained in the support base defined by $\mathbf{h}_j$ (highlighted in Fig. 2). In the numerical optimisation, this constraint is expressed by introducing the vector $\mathbf{b}_j = [b_{\mathrm{x},j}, b_{\mathrm{y},j}, 0.0]$ that connects the horizontal projection of support j to $\mathbf{h}_j$.

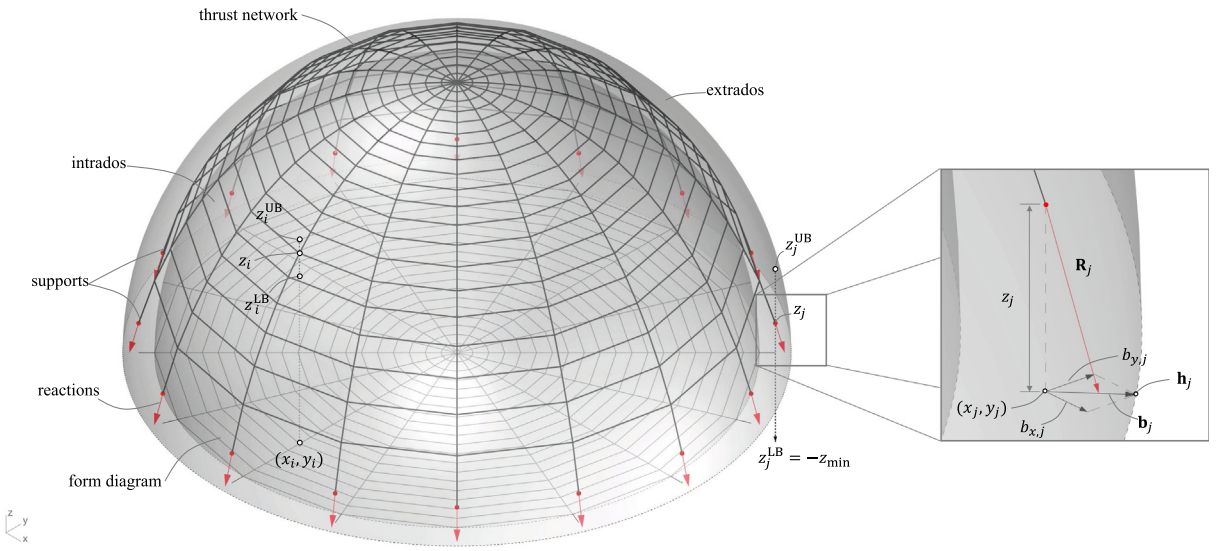

Fig. 2. Thrust network obtained from a (fixed in plane) form diagram where support vertices and reactions (or thrusts) are highlighted in red. The admissibility criteria is highlighted: the height of each internal i, and a support j vertex must be constrained among intrados (z_i^{LB} or z_j^{LB}) and extrados (z_i^{UB} or z_j^{UB}), and a special treatment is given to supports that have no projection in the intrados by considering the parameter z_{min}. Additionally, the thrust exerted on each support $\mathbf{R}_j$ must not cross the limit of the extrados $\mathbf{h}_j$. (For interpretation of the references to color in this figure legend, the reader is referred to the web version of this article.)

4. Formulation of nonlinear optimisation problems

Following the formulation presented in Section 3, this Section frames the search for specific thrust networks described in 2.3 as nonlinear constrained optimisation problems (NLPs).

Section 4.1 formulates the optimisation required to find the extreme minimum and maximum horizontal thrusts of a given form diagram and a given masonry envelope. Section 4.2 formulates the optimisation required to find the minimum thickness, which requires that the constraints are modified to consider the variable boundary geometry of the thrust networks. The minimum thickness problem (4.2) is presented for analytically described geometries in Section 4.2.1, and strategies to cope with the case of non-analytic geometries are discussed in Section 4.2.2. Section 4.3 gives details about the nonlinear solver used, and Section 4.4 briefly discusses the influence of different starting points.

4.1. Min-max thrust optimisation

The first optimisation problem refers to the minimisation and maximisation (min-max) of the horizontal thrust subjected to the limit analysis' admissibility criteria.

The variables of the optimisation are the independent force densities $\mathbf{q}_{ind}$ and the height of the supports $\mathbf{z}_b$ used to describe the internal vertex heights $\mathbf{z}_i$ computed per Eq. (3). The objective function f_1 for this problem (6a) is the sum of the norm of the horizontal reactions $R_{x,j}$, and $R_{y,j}$ at each support j computed per Eqs. (4a) and (4b). This objective function is linear and depends exclusively on the independent force densities $\mathbf{q}_{ind}$. The positive form of f_1 minimises the horizontal components of the thrust, providing the minimum (or passive) thrust state for the vault (Fig. 1b). Conversely, the negative form ($-f_1$) maximises the thrust on the structure, finding the maximum (or active) state (Fig. 1c). The NLP can be expressed as follows:

$$\underset{\mathbf{q}_{ind}, \mathbf{z}_b}{\text{minimise}} \quad f_1 = \pm \sum_{j=1}^{n_b} \sqrt{R_{x,j}^2 + R_{y,j}^2}, \tag{6a}$$

$$\text{subject to} \quad \mathbf{q}_{dep} \geqslant \mathbf{0}, \tag{6b}$$

$$z_i^{LB} \leqslant z_i(\mathbf{q}_{ind}, \mathbf{z}_b) \leqslant z_i^{UB}, \quad \text{for} \quad i = 1, 2, \dots n, \tag{6c}$$

$$|b_{x,j}| - \left|\frac{R_{x,j}}{R_{z,j}}\right| * z_{b,j} \geqslant 0, \quad \text{for} \quad j = 1, 2, \dots n_b, \tag{6d}$$

$$|b_{y,j}| - \left|\frac{R_{y,j}}{R_{z,j}}\right| * z_{b,j} \geqslant 0, \quad \text{for} \quad j = 1, 2, \dots n_b, \tag{6e}$$

$$0 \leqslant q_{ind,l} \leqslant q_{max}, \quad \text{for} \quad l = 1, 2, \dots k, \tag{6f}$$

with:

- constraint (6b) modelling the unilateral behaviour, i.e., the vector of dependent force densities ($\mathbf{q}_{dep}$) from Eq. (5) must be non-negative;
- nonlinear constraint (6c) imposing that the vertices of the thrust network z_i are contained within the upper and lower bounds of the masonry z_i^{UB} and z_i^{LB} respectively;
- nonlinear constraints (6d) and (6e) requiring that the force exerted on each support does not cross the limit of the extrados ($\mathbf{h}_j$) defined by the components $b_{x,j}$ and $b_{y,j}$ (see Fig. 2). More specifically, the support rise ($z_{b,j}$) times the reaction slopes ($|R_{x,j}/R_{z,j}|$, or $|R_{y,j}/R_{z,j}|$) must be bounded by $|b_{x,j}|$, or $|b_{y,j}|$. The absolute values are considered since $R_{x,j}$ and $R_{y,j}$ or $b_{x,j}$ and $b_{y,j}$ may assume positive or negative values according to the position (x_i, y_i) of the support in the plane;
- constraint (6f) bounding the independent force densities $\mathbf{q}_{ind}$ to be positive and limited by the parameter $q_{max} > 0$.

In the present formulation, gradient and jacobian matrices are obtained analytically and are described herein.

The gradient of f_1 is a function of the independent force densities only, and each of the scalar component j of $\partial f_1 / \partial \mathbf{q}_{ind}$, repre-

senting the sensibility of the objective function with respect to the j-th independent force density can be obtained by applying the chain rule as:

$$\left(\frac{\partial f_1}{\partial \mathbf{q}_{\text{ind}}}\right)_j = \left(\frac{\partial f_1}{\partial \mathbf{q}}\frac{\partial \mathbf{q}}{\partial \mathbf{q}_{\text{ind}}}\right)_j = \pm\sum_i^{n_b}\frac{R_{x,i}\left(\frac{\partial \mathbf{R}_x}{\partial \mathbf{q}_{\text{ind}}}\right)_{i,j} + R_{y,i}\left(\frac{\partial \mathbf{R}_y}{\partial \mathbf{q}_{\text{ind}}}\right)_{i,j}}{\sqrt{R_{x,i}^2 + R_{y,i}^2}}, \tag{7}$$

where the sign $\pm$ reflects the minimisation of maximisation of the thrust, the notation $()_{i,j}$ represents the (i,j) matrix element, and the terms $\partial \mathbf{R}_x/\partial \mathbf{q}_{\text{ind}}$ and $\partial \mathbf{R}_y/\partial \mathbf{q}_{\text{ind}}$ $[n_b \times k]$ are computed by Eqs. (9a) and (9b). To simplify notation, the derivative $\partial \mathbf{q}/\partial \mathbf{q}_{\text{ind}}$ is denoted $\partial \mathbf{Q}$ $[m \times k]$ and can be computed by blocks as:

$$\partial \mathbf{Q} = \frac{\partial \mathbf{q}}{\partial \mathbf{q}_{\text{ind}}} = \begin{bmatrix} \frac{\partial \mathbf{q}_{\text{dep}}}{\partial \mathbf{q}_{\text{ind}}} \\ \frac{\partial \mathbf{q}_{\text{ind}}}{\partial \mathbf{q}_{\text{ind}}} \end{bmatrix} = \begin{bmatrix} -\mathbf{E}_{\text{dep}}^{\dagger}\mathbf{E}_{\text{ind}} \\ \mathbf{I}_k \end{bmatrix}, \tag{8}$$

where $\mathbf{I}_k$ represents the k-dimensional identity matrix. It follows that the derivatives of the horizontal reaction can be written as:

$$\frac{\partial \mathbf{R}_x}{\partial \mathbf{q}_{\text{ind}}} = \frac{\partial \mathbf{R}_x}{\partial \mathbf{q}}\frac{\partial \mathbf{q}}{\partial \mathbf{q}_{\text{ind}}} = \mathbf{C}_b^T\mathbf{U}\partial\mathbf{Q}, \tag{9a}$$

$$\frac{\partial \mathbf{R}_y}{\partial \mathbf{q}_{\text{ind}}} = \frac{\partial \mathbf{R}_y}{\partial \mathbf{q}}\frac{\partial \mathbf{q}}{\partial \mathbf{q}_{\text{ind}}} = \mathbf{C}_b^T\mathbf{V}\partial\mathbf{Q}. \tag{9b}$$

The jacobian matrix is computed for the constraints by applying the chain rule. The constraint on the height of the free vertices (6b) requires the application of the chain rule to Eq. (3). As the self-weight $\mathbf{p}_z$ is based on the projection of the network on the middle surface of the masonry, the weights are computed only at the beginning of the problem and do not change with the heights of the thrust network ($\partial \mathbf{p}_z/\partial \mathbf{z} = \mathbf{0}$). Therefore, the vector $\partial \mathbf{z}_i/\partial \mathbf{q}_{\text{ind}}$ $[n_i \times k]$ is computed as:

$$\frac{\partial \mathbf{z}_i}{\partial \mathbf{q}_{\text{ind}}} = \frac{\partial \mathbf{z}_i}{\partial \mathbf{q}}\frac{\partial \mathbf{q}}{\partial \mathbf{q}_{\text{ind}}} = -(\mathbf{C}_i^T\mathbf{Q}\mathbf{C}_i)^{-1}\mathbf{C}_i^T\mathbf{W}\partial\mathbf{Q}, \tag{10}$$

and, similarly, the vector $\partial \mathbf{z}_i/\partial \mathbf{z}_b$ $[n_i \times n_b]$ can also be computed deriving Eq. (3) as follows:

$$\frac{\partial \mathbf{z}_i}{\partial \mathbf{z}_b} = -(\mathbf{C}_i^T\mathbf{Q}\mathbf{C}_i)^{-1}\mathbf{C}_i^T\mathbf{Q}\mathbf{C}_b. \tag{11}$$

Regarding the partial derivatives of constraints (6d) and (6e), let $F_{x,i}$ denote the left side of constraint (6d) for each support i. It is of interest to define the derivatives of the vertical reaction with respect to the problem variables $\mathbf{R}_z/\mathbf{q}_{\text{ind}}$ $[n_b \times k]$ and $\mathbf{R}_z/\mathbf{z}_b$ $[n_b \times n_b]$ as:

$$\frac{\partial \mathbf{R}_z}{\partial \mathbf{q}_{\text{ind}}} = \mathbf{C}_b^T\mathbf{W}\partial\mathbf{Q} + \mathbf{C}_b^T\mathbf{Q}\mathbf{C}\begin{bmatrix} \frac{\partial \mathbf{z}_i}{\partial \mathbf{q}_{\text{ind}}} \\ \mathbf{0} \end{bmatrix}, \tag{12a}$$

$$\frac{\partial \mathbf{R}_z}{\partial \mathbf{z}_b} = \mathbf{C}_b^T\mathbf{Q}\mathbf{C}\begin{bmatrix} \frac{\partial \mathbf{z}_i}{\partial \mathbf{z}_b} \\ \mathbf{I}_{n_b} \end{bmatrix}, \tag{12b}$$

and with these, it follows that $\partial F_{x,i}/\partial \mathbf{z}_b$ can be expressed as the column vector $[n_b \times 1]$:

$$\frac{\partial F_{x,i}}{\partial \mathbf{z}_b} = -\left|\frac{R_{x,i}}{R_{z,i}}\right|(\mathbf{I}_{n_b})_i^T - \frac{z_{b,i}|R_{x,i}|}{R_{z,i}^2}\left(\frac{\partial \mathbf{R}_z}{\partial \mathbf{z}_b}\right)_i^T, \tag{13}$$

where the notation $()_i$ represents a slice in the i-th line of matrices, resulting in a vector of size $[1 \times n_b]$. The term $\partial F_{x,i}/\partial \mathbf{q}_{\text{ind}}$ can be expressed as the column vector $[k \times 1]$ in Eq. (14), where the $\pm$ sign reflects the sign of $R_{x,i}$:

$$\frac{\partial F_{x,i}}{\partial \mathbf{q}_{\text{ind}}} = -\frac{z_{b,i}}{R_{z,i}^2}\left(|R_{x,i}|\left(\frac{\partial \mathbf{R}_z}{\partial \mathbf{q}_{\text{ind}}}\right)_i \pm |R_{z,i}|\left(\frac{\partial \mathbf{R}_x}{\partial \mathbf{q}_{\text{ind}}}\right)_i\right)^T, \tag{14}$$

and an analogous procedure is applied to constraint (6e) to find the derivatives with respect to the y-direction.

The formulation presented in this chapter allows for computing minimum and maximum thrusts for TNs described by a fixed form diagram projection and constrained to a geometrical envelope and reaction bounds. This formulation is a sequence of a previously published paper [29], improved with the analytical description of the sensitivities. The formulation is similar to the one described in [24] with the addition of constraints 6d and 6e and reformulation to describe the geometry of the structure based on its middle surface.

4.2. Minimum thickness optimisation

As discussed in Section 2.3, finding the minimum thickness is relevant to compute the GSF. This section shows how the optimisation problem (6a-6f) can be modified to such an aim. In Section 4.2.1, cases in which the bounds of the structure are known analytically are presented. Subsequently, strategies to cope with the case of non-analytically describable surfaces are discussed in Section 4.2.2.

4.2.1. Analytical formulation of minimum thickness

This section is devoted to structures that can be described analytically from a shape function describing the middle surface of the structure and a thickness applied orthogonally to this middle surface. To this aim, three multi-variable functions are defined to model a given structure: $s_m(x_i, y_i), s_{LB}(x_i, y_i, t)$, and $s_{UB}(x_i, y_i, t)$ representing the middle, the intrados, or lower-bound (LB), and extrados, or upper-bound (UB). One example of such an analytical surface is the dome studied in Section 5.1 and described through Eqs. 21a, 21b and 21c. Once the intrados and extrados of the geometry can be described as a function of the thickness parameter t of the masonry structure, the problem can be written by using the objective function f_2 as below:

$$\underset{\mathbf{q}_{\text{ind}},\mathbf{z}_b,t}{\text{minimise}} \quad f_2 = t, \tag{15a}$$

$$\text{subject to} \quad \mathbf{q}_{\text{dep}} \geqslant \mathbf{0}, \tag{15b}$$

$$z_i^{LB}(t) \leqslant z_i(\mathbf{q}_{\text{ind}}, \mathbf{z}_b) \leqslant z_i^{UB}(t), \quad \text{for} \quad i = 1, 2, \ldots n, \tag{15c}$$

$$b_{x,j}(t) - \left|\frac{R_{x,j}}{R_{z,j}}\right| * z_{b,j} \geqslant 0, \quad \text{for} \quad j = 1, 2, \ldots n_b, \tag{15d}$$

$$b_{y,j}(t) - \left|\frac{R_{y,j}}{R_{z,j}}\right| * z_{b,j} \geqslant 0, \quad \text{for} \quad j = 1, 2, \ldots n_b, \tag{15e}$$

$$0 \leqslant q_{\text{ind},l} \leqslant q_{\max}, \quad \text{for} \quad l = 1, 2, \ldots k, \tag{15f}$$

$$t \geqslant 0, \tag{15g}$$

with:

- nonlinear constraint (15c) expressing the heights of intrados $z_{i,i}^{LB}(t)$ and extrados $z_{i,i}^{UB}(t)$ as a function of the structural thickness t using the shape functions $s_{LB}(x_i, y_i, t)$ and $s_{UB}(x_i, y_i, t)$ computed at the horizontal coordinates (x_i, y_i) of vertex i;
- nonlinear constraints (15d) and (15e) requiring that the thrust on the support does not cross the extrados, as in 6d and 6e, with the difference that the geometry parameters $b_{x,j}(t)$ and $b_{y,j}(t)$ are here defined also as a function of the structural thickness t;
- constraint (15f) bounding the independent force densities to be positive and limited by the maximum force density parameter $q_{\max}$; and
- constraint (15g) bounding the parameter t to be positive. If the optimum value of t is higher than the vault's original thickness t_0 the structure is unstable. In that case, the resulting minimum thickness can give an idea of how far the structure is from a stable thickness.

Regarding the sensitivities, the additional variable t adds a column to the jacobian matrix. This column influences constraints 15c, 15d and 15e. Therefore, the only modification is the addition of the column vectors $\partial \mathbf{z}^{\mathrm{UB}}/\partial t$ and $\partial \mathbf{z}^{\mathrm{LB}}/\partial t$ $[n \times 1]$ representing the sensitivities on the upper and lower bonds with regards to a change in the thickness parameter t. Similarly, the sensitivity of parameters b_x, and b_y also enter the jacobian matrix with the column vectors $\partial \mathbf{b}_x/\partial t$ and $\partial \mathbf{b}_y/\partial t$ $[n_b \times 1]$. These derivatives depend upon the shape defined.

The gradient of the objective function is not a function of either $\mathbf{q}_{\mathrm{ind}}$ or $\mathbf{z}_b$, and its derivative with respect to the structural thickness is $\partial f_2/\partial t = 1$.

The present methodology enables finding the minimum thickness as a direct optimisation and can be applied to any shape once a closed-form representation of the intrados and extrados is known and can be expressed by the functions $s_{\mathrm{LB}}(x_i, y_i, t)$ and $s_{\mathrm{UB}}(x_i, y_i, t)$ mentioned above. However, to cope with cases where intrados and extrados can not be analytically described, which arise when assessing existing masonry structures, the following section discusses an approach for general surfaces, e.g. those described by a point cloud.

4.2.2. General formulation of minimum thickness

This section introduces the numerical strategies used to describe the relevant surfaces (intrados, extrados and middle surfaces) as approximated offset meshes. There are multiple ways to define a perpendicular offset of a piecewise smooth surface [49,50]. In the present formulation, this offset is linear and takes its direction from the normal unit vectors $\hat{\mathbf{n}}_i$ of each surface.

This paper presents two different strategies, called A and B, to deal with offsets, based on the available information about the structural geometry. Strategy A (Fig. 3a) considers that the elevation $\bar{z}_i^{\mathrm{m}}$ of the middle surface Σ^{m} on each vertex (x_i, y_i) of the form diagram is known. The new intrados z_i^{LB} and extrados z_i^{UB} bounds are computed as a function of the half-thickness $t/2$ through opposite offsets along the direction of the middle surface's unit normal vectors $\hat{\mathbf{n}}_i^{\mathrm{m}}$. Conversely, strategy B (Fig. 3b) assumes that intrados Σ^{LB} and extrados Σ^{UB} surfaces are known with elevations $\bar{z}_i^{\mathrm{LB}}$ and $\bar{z}_i^{\mathrm{UB}}$, respectively. The new bounds are computed through an offset in the direction of the normal vectors $\hat{\mathbf{n}}_i^{\mathrm{LB}}$ and $\hat{\mathbf{n}}_i^{\mathrm{UB}}$, respectively, to the interior of the structural domain, considering the offset distance α. For both strategies, the offset is computed linearly by projecting the normal vectors $\hat{\mathbf{n}}_i = [\hat{n}_{x,i}, \hat{n}_{y,i}, \hat{n}_{z,i}]$ perpendicularly onto the vertical direction. The magnitude of the vertical projection $\mathrm{proj}_k(\hat{\mathbf{n}}_i)$ is computed by Eq. (16) as a function of $\hat{\mathbf{n}}_i$.

$$\mathrm{proj}_k(\hat{\mathbf{n}}_i) = \sqrt{1 + \frac{\hat{n}_{x,i}{}^2 + \hat{n}_{y,i}{}^2}{\hat{n}_{z,i}{}^2}}. \tag{16}$$

By considering the vertical projections in the offsets, the new bounds corresponding to each vertex (x_i, y_i) in the form diagram can be calculated directly. The position of the bounds may present a deviation from the exact position if an analytical curved description was available, and this deviation is larger in vertical portions of the structure, i.e., close to its springings. The application in Section 5.2 on cross vaults analyses such deviations. The optimisation problems for the two strategies are formalised below:

Strategy A: from middle surface

The optimisation problem starting from the middle surface Σ^{m}, defined by heights $\bar{z}_i^{\mathrm{m}}$ for the i vertices of the form diagram (Fig. 3a) is defined in Eqs. (17):

$$\underset{\mathbf{q}_{\mathrm{ind}}, \mathbf{z}_b, t}{\text{minimise}} \quad f_2 = t, \tag{17a}$$

$$\text{subject to} \quad \mathbf{q}_{\mathrm{dep}} \geqslant \mathbf{0}, \tag{17b}$$

$$z_i^{\mathrm{LB}}(t) = \bar{z}_i^{\mathrm{m}} - \frac{t}{2}\mathrm{proj}_k(\hat{\mathbf{n}}_i^{\mathrm{m}}), \quad \text{for} \quad i = 1, 2, \ldots n, \tag{17c}$$

$$z_i^{\mathrm{UB}}(t) = \bar{z}_i^{\mathrm{m}} + \frac{t}{2}\mathrm{proj}_k(\hat{\mathbf{n}}_i^{\mathrm{m}}), \quad \text{for} \quad i = 1, 2, \ldots n, \tag{17d}$$

$$z_i^{\mathrm{LB}}(t) \leqslant z_i(\mathbf{q}_{\mathrm{ind}}, \mathbf{z}_b) \leqslant z_i^{\mathrm{UB}}(t), \quad \text{for} \quad i = 1, 2, \ldots n, \tag{17e}$$

$$0 \leqslant q_{\mathrm{ind},l} \leqslant q_{\max}, \quad \text{for} \quad l = 1, 2, \ldots k, \tag{17f}$$

$$t \geqslant 0. \tag{17g}$$

The optimisation minimises the thickness t and constraint (17e) bounds the heights z_i taking into account the normal unit vectors $\hat{\mathbf{n}}_i^{\mathrm{m}}$ as illustrated in Fig. 3a. This procedure could be modified to take into account structures with variable thickness by properly modifying constraints (17c) and (17d).

The gradient of the objective function (17a) is the same as in the previous problem, and the jacobian matrix is added with the column vectors considering the influence of the thickness t to the bounds on the heights of the vertices. For each vertex i, this is computed as:

$$\frac{\partial z_i^{\mathrm{LB}}}{\partial t} = -\frac{1}{2}\mathrm{proj}_k(\hat{\mathbf{n}}_i^{\mathrm{m}}) \tag{18a}$$

$$\frac{\partial z_i^{\mathrm{UB}}}{\partial t} = \frac{1}{2}\mathrm{proj}_k(\hat{\mathbf{n}}_i^{\mathrm{m}}) \tag{18b}$$

Strategy B: from intrados and extrados

The optimisation problem starting from intrados and extrados is formulated herein considering $\bar{z}_i^{\mathrm{UB}}$ and $\bar{z}_i^{\mathrm{LB}}$ for the i vertices of the form diagram. The variable α representing the offset magnitude from intrados and extrados is introduced (Fig. 3b). To minimise the thickness, the objective function f_3 maximises α, and the optimisation problem can be written as:

$$\underset{\mathbf{q}_{\mathrm{ind}}, \mathbf{z}_b, \alpha}{\text{maximise}} \quad f_3 = \alpha, \tag{19a}$$

$$\text{subject to} \quad \mathbf{q}_{\mathrm{dep}} \geqslant \mathbf{0}, \tag{19b}$$

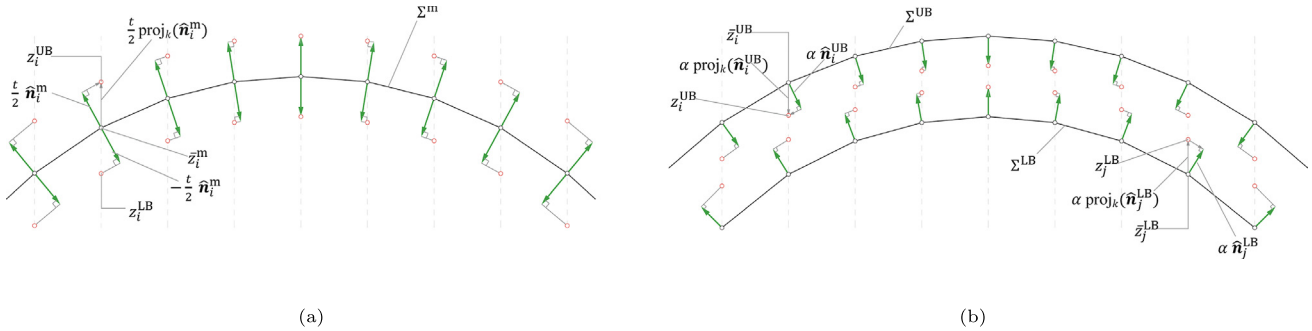

(a) (b)

Fig. 3. Two different offset strategies as from the available geometrical information: (a) strategy A considering a known middle surface Σ^{m}, of heights $\bar{z}_i^{\mathrm{m}}$, and obtaining extrados z_i^{UB} and intrados z_i^{LB} by offsetting Σ^{m} up and down of half-thickness $t/2$ along $\mathrm{proj}_k(\hat{\mathbf{n}}_i^{\mathrm{m}})$ defined as function of the normal vectors $\hat{\mathbf{n}}_i^{\mathrm{m}}$; (b) strategy B considering known outer surfaces Σ^{LB}, and Σ^{UB}, defined at $\bar{z}_i^{\mathrm{LB}}$ and $\bar{z}_i^{\mathrm{UB}}$, used to obtain the new bounds by offsetting these surfaces along $\mathrm{proj}_k(\hat{\mathbf{n}}_i^{\mathrm{LB}})$ and $\mathrm{proj}_k(\hat{\mathbf{n}}_i^{\mathrm{UB}})$, defined as function of the unit normal vectors $\hat{\mathbf{n}}_i^{\mathrm{LB}}$ and $\hat{\mathbf{n}}_i^{\mathrm{UB}}$ considering the offset magnitude α.

$$z_i^{\mathrm{LB}}(\alpha) = \bar{z}_i^{\mathrm{LB}} + \alpha \mathrm{proj}_{\hat{k}}(\hat{\mathbf{n}}_i^{\mathrm{LB}}), \quad \text{for} \quad i = 1, 2, \ldots n, \tag{19c}$$
$$z_i^{\mathrm{UB}}(\alpha) = \bar{z}_i^{\mathrm{UB}} - \alpha \mathrm{proj}_{\hat{k}}(\hat{\mathbf{n}}_i^{\mathrm{LB}}), \quad \text{for} \quad i = 1, 2, \ldots n, \tag{19d}$$
$$z_i^{\mathrm{LB}}(\alpha) \leqslant z_i(\mathbf{q}_{\mathrm{ind}}, \mathbf{z}_{\mathrm{b}}) \leqslant z_i^{\mathrm{UB}}(\alpha), \text{for} \quad i = 1, 2, \ldots n, \tag{19e}$$
$$0 \leqslant q_{\mathrm{ind},l} \leqslant q_{\max}, \quad \text{for} \quad l = 1, 2, \ldots k, \tag{19f}$$
$$\alpha \in \mathbb{R}. \tag{19g}$$

Once the maximum offset $\alpha_{\max}$ is found, the minimum thickness is calculated as $t_{\min} = t_0 - 2 * \alpha_{\max}$ for the initial constant thickness t_0. As in the previous problem, this procedure could be modified to take into account structures with variable thickness by properly modifying constraints (19c) and (19d).

The gradient of the objective function is not a function of either $\mathbf{q}_{\mathrm{ind}}$ or $\mathbf{z}_{\mathrm{b}}$, and its derivative with respect to α is $\partial f_3/\partial\alpha = 1$. The jacobian matrix is added with the column vectors considering the influence of α to the bounds on the heights of each vertex i as:

$$\frac{\partial z_i^{\mathrm{LB}}}{\partial \alpha} = \mathrm{proj}_{\hat{k}}(\hat{\mathbf{n}}_i^{\mathrm{LB}}) \tag{20a}$$
$$\frac{\partial z_i^{\mathrm{UB}}}{\partial \alpha} = -\mathrm{proj}_{\hat{k}}(\hat{\mathbf{n}}_i^{\mathrm{UB}}) \tag{20b}$$

The problems defined in this Section are computationally efficient and allow for computing the minimum thickness, and consequently, the GSF of non-analytically described geometries. In Section 5.3, these surfaces will be obtained from point clouds, which are common outputs from laser scanner surveys from ancient masonry buildings.

4.3. Nonlinear solvers

Although the NLPs described in Sections 4.1 and 4.2 have linear objective functions, the constraints set on the heights of the vertices of the form diagram are nonlinear, calculated via Eq. (3) from the variables $\mathbf{q}_{\mathrm{ind}}$ and $\mathbf{z}_{\mathrm{b}}$, requiring the inverse of the matrix $\mathbf{D}_{\mathrm{i}}^{-1} = (\mathbf{C}_{\mathrm{i}}^{\mathrm{T}}\mathbf{Q}\mathbf{C}_{\mathrm{i}})^{-1}$.

This paper implements a version of the Sequential Least Squares Programming (SLSQP) [33], available in the open-source Python library Scipy [51]. This solver linearises the constraints at each iteration, dealing efficiently with the hard constraints in the heights, $\mathbf{z}_{\mathrm{i}}$. This solver allows finding an optimum solution for most of the problems in a few seconds.

The numerical problem is set up and solved within a python environment through the COMPAS framework [32].

4.4. Starting points

Due to the nonlinear nature of the problems described, the choice of starting point influences the convergence time and the solvability of the examples. The starting point does not need to always be feasible. However, it has been observed that starting from an equilibrated distribution of compressive-only force densities is strictly necessary to solve the optimisation problems with SLSQP. To that end, a preconditioning optimisation is adopted to minimise the load-path, as in [52].

5. Numerical applications

A series of numerical applications, with increasing complexity, are presented herein. First, the case of a hemispherical dome having a known analytical description is discussed (Section 5.1), which allows benchmarking the present methodology against different approaches. Section 5.2 presents the example of a cross vault, where both cases- analytic and non-analytic geometry descriptions - are compared. The last example (Section 5.3) presents how the strategy could be applied in a practical assessment scenario, in which the geometry is obtained from a point cloud. Together the examples show the flexibility of the methodology and its scope of application.

When reported, the time required to solve the optimisation problems is computed from a laptop with 2.2 GHz Intel Core i7 (I7-8750H) and 16 GB of RAM.

5.1. Hemispherical dome

The first numerical application looks at a hemispheric dome described analytically by the thickness parameter t. The dome's geometry is defined by an initial thickness $t_0 = 0.50$,m, radius $r = 5.00$,m (i.e., $t_0/r = 0.10$), and centre at point $(x_c, y_c, 0.0) = (5.0, 5.0, 0.0)$. In this case, the functions $s_{\mathrm{m}}, s_{\mathrm{LB}}$ and s_{UB} representing middle, lower-bound, and upper-bound can be described for every point i in the form diagram with planar coordinates $(x_{\mathrm{i}}, y_{\mathrm{i}})$ as:

$$s_{\mathrm{m}}(x_i, y_i) = \sqrt{r^2 - (x_i - x_c)^2 - (y_i - y_c)^2} \tag{21a}$$

$$s_{\mathrm{UB}}(x_i, y_i, t) = \sqrt{(r + t/2)^2 - (x_i - x_c)^2 - (y_i - y_c)^2} \tag{21b}$$

$$s_{\mathrm{LB}}(x_i, y_i, t) = \begin{cases} \sqrt{(r - t/2)^2 - (x_i - x_c)^2 - (y_i - y_c)^2} & \text{if } (x_i - x_c)^2 - (y_i - y_c)^2 \leqslant (r - t/2)^2 \\ -z_{\min} & \text{otherwise} \end{cases} \tag{21c}$$

The dome has weight density $\gamma = 20\ \mathrm{kN/m^3}$. The self-weight is computed considering the area of the dome's middle surface and its thickness, resulting in a total self-weight $W_0 = 1570$ kN. The geometry of the dome obtained with thickness-over-radius $t_0/r = 0.10$ is depicted in Fig. 4.

5.1.1. Form diagrams considered

The form diagram topology is chosen to represent the meridian and hoop stresses which are known to appear in domes [7,25,9]. For a given topology, the discretisation level will define the geometry of the form diagram. The discretisation will be parametrically defined by the tuple $(n_{\mathrm{P}}, n_{\mathrm{M}})$, with the first representing the number parallels (or hoops) while the second the number of meridians (Fig. 5). To capture the influence of the mesh discretisation, a sensitivity study varying the parameters $(n_{\mathrm{P}}, n_{\mathrm{M}})$ will be carried out. Specifically, the number of parallels n_{P} will be varied from 4 to 24, in steps of four, while the number of meridians n_{M} from 12 to 24, also in steps of four, to total 24 different diagrams. Supports are assigned to the vertices on the perimeter of the diagram. The

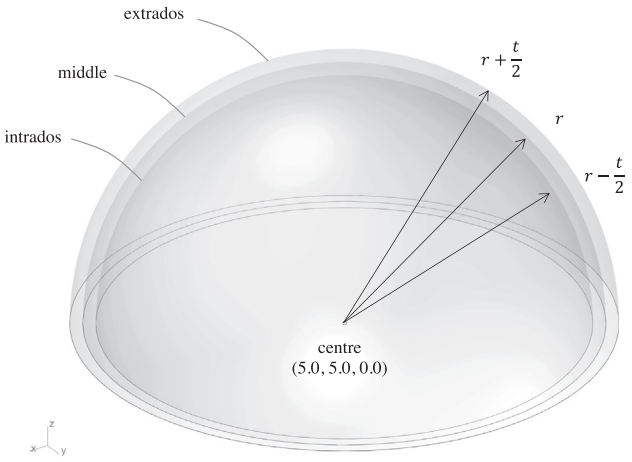

Fig. 4. Intrados, middle and extrados surfaces of the hemispheric dome having thickness-over-radius $t_0/r = 0.10$.

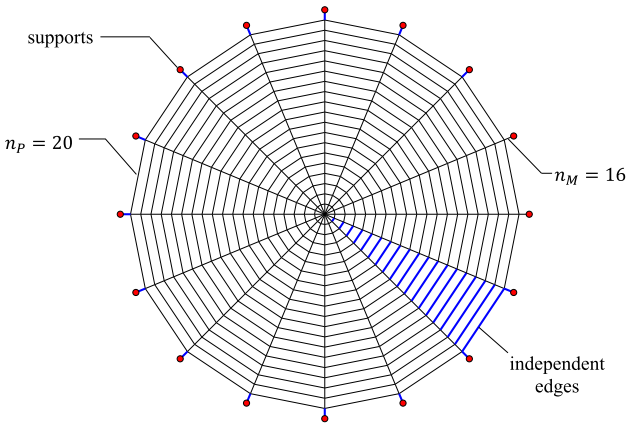

Fig. 5. Form diagram obtained with 20 parallels n_P, and 16 meridians n_M and highlight in its independent edges (blue) and supports (red). (For interpretation of the references to color in this figure legend, the reader is referred to the web version of this article.)

form diagram obtained with $(n_P, n_M) = (20, 16)$ is depicted in Fig. 5. This diagram is composed of 640 edges, from which 33 are independent (blue).

5.1.2. Analytical approach to minimum thickness

The optimisation presented in Section 4.2.1 is executed for 24 discretisation levels. The objective function minimises the thickness of the structure (Eqs. (15a-15g)), starting from the initial thickness $t_0 = 0.50$ m. Constraints are applied in the height of all the vertices, requiring that they remain between the intrados and extrados of the dome described by Eqs. (21b) and (21c). Specifically, $z_{min} = 0.0$ is assumed for these analyses. The starting point for each optimisation is the minimum load-path solution, as defined in Section 4.4. As a benchmark, the results are compared with the minimum thickness of a masonry hemispherical dome obtained by Heyman [25] using membrane equations and validated recently in [9]. Particularly, using the adimensional parameter thickness-over-radius, the minimum thickness obtained in [25] is $t_{min}/r = 0.042$. The results of minimum thickness-over-radius for the 20 discretisation levels are presented in Fig. 6.

The results obtained in this analysis show that only the number of parallels n_P affects the minimum thickness value, since the graph of Fig. 6 shows that the solutions corresponding to different n_M values collapse to the same curve. Moreover, the results

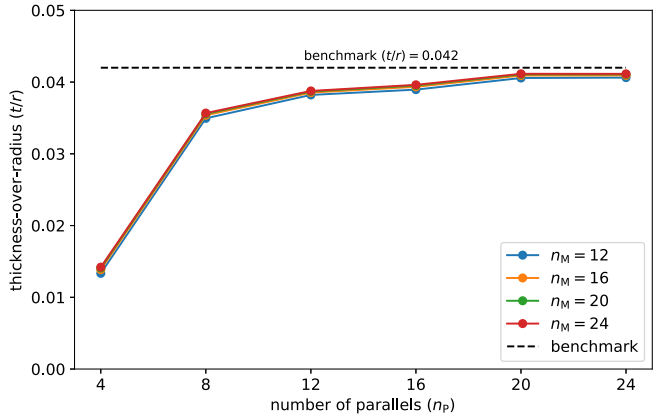

Fig. 6. Minimum thickness sensitivity study for the 24 discretisation levels considered. Curves are grouped according to the number of meridians n_M.

obtained are always under-conservative, since the minimum thickness calculated is inferior to the theoretical minimum thickness from [25]. This deviation is larger for coarse discretisations ($n_P = 4$), meaning that these are not appropriate to model the dome problem. However, the deviation decreases with denser form diagrams, resulting in errors lower than 2% for $n_P \geqslant 20$. The computational burden needed to solve the optimisation problems of the present sensitivity study are reported in Table 1. The solving time varies from 0.1 to 1.9 s, depending on the discretisation (n_P, n_M) level.

The solution of the minimum thickness problem for $(n_P, n_M) = (20, 16)$ is depicted in Fig. 7. On such plots, the unloaded edges are excluded, while the thickness of the remaining edges is proportional to the force carried and computed as the product of the force-density times the length of the edge, namely $f_i = q_i * l_i$. In addition, the vertices touching the intrados are denoted with blue dots while the ones touching the extrados are labelled in green. The minimum thickness-over-span obtained for this problem is $t_{min}/r = 0.041$, and the GSF of this structure is equal to $GSF = t_0/t_{min} = 2.44$.

Regarding the internal distribution of the forces in the minimum thickness solution (Fig. 7), a bi-axial compressive cap is observed in the upper portion of the dome and a uniaxial stress state forms towards the supports, where the hoop forces vanish. The height of the supports is $z_b = +0.421$ m in a position such that the vector of the reaction forces extends to the outer perimeter of the dome (see Fig. 7c). The forces inside the structure vary from 0.0 kN (in the edges that are not drawn) to 84.6 kN. In the perimeter of the top compressive cap, the thrust network touches the extrados of the structure, and close to the base, it touches the intrados. Such a stress field is compatible with Heyman's 'orange slice' mechanism proposed in [25] for an outward (passive) radial displacement of the supports. In the following section, we will discuss the extremes, minimum and maximum thrusts for the initial thickness of the structure $t_0/r = 0.10$.

5.1.3. Construction of the stability domain

As discussed in Section 2.2.2 and initially presented in [29], besides defining the minimum thickness, or GSF, the stability domain of a masonry vault can give information about the size of the domain of admissible stress states and robustness of the structure. The domain is obtained by computing minimum and maximum thrusts for values of thickness between the initial and the limit thicknesses.

The process is executed for $(n_P, n_M) = (20, 16)$. From the minimum thickness obtained, a sequential optimisation is performed for increasing values of thickness. At each step, the loads are scaled to reflect the new thickness, and the minimum (T_i^{min}) and maximum (T_i^{max}) thrusts are computed and plotted in the graph of Fig. 8 as a percentage of the self-weight at each step (W_i). This graph represents the stability domain of this structure, limited by the lines of maximum (red) and minimum (blue) thrust meeting at the limit state. We observe that the stability domain shrinks parabolically towards the limit state, which gives an idea of the drop of the stability for reduced values of thickness.

From the stability domain of Fig. 8, we can check that the minimum and maximum thrusts for the initial state, $t_0/r = 0.10$, correspond to $(T/W)_{min} = 19.9\%$ and $(T/W)_{max} = 62.6\%$. In the limit state, $(T/W)_{limit} = 24.3\%$.

The minimum and maximum thrust states are depicted in Figs. 9 and 10, respectively. The minimum thrust state (Fig. 9) returns a solution that is qualitatively the same as the one from the minimum thickness solution (Fig. 7), which again reflects Heyman's 'orange slice' mechanism for an outward (passive) radial displacement of the supports. In this mechanism, cracks form

Table 1
Solving times [sec] for the minimum thickness problem assuming different discretisation tuples (n_P, n_M).

	n_M			
n_P	12	16	20	24
4	0.1	0.2	0.2	0.3
8	0.2	0.2	0.2	0.2
12	0.2	0.3	0.4	0.5
16	0.2	0.3	0.5	0.7
20	0.8	1.6	1.7	1.9
24	0.4	0.6	0.8	1.1

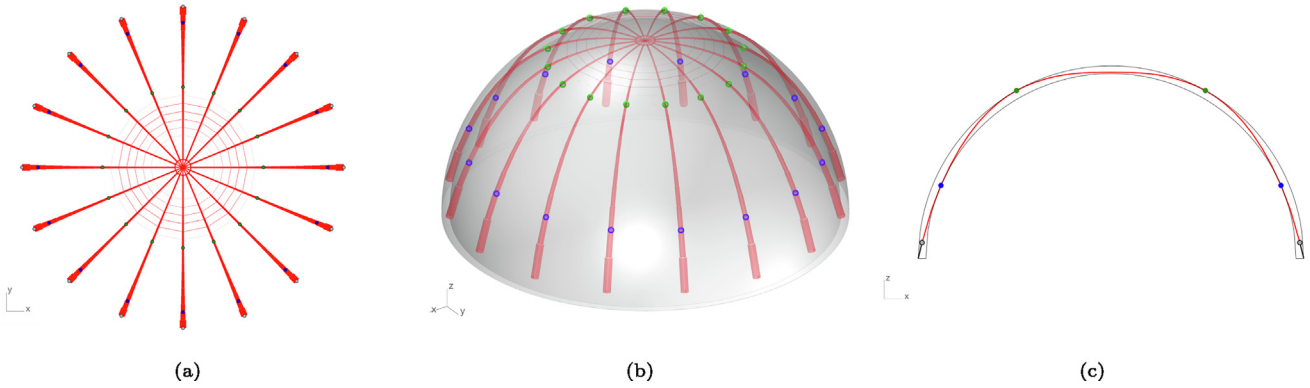

Fig. 7. Minimum thickness solution obtained for $(n_P, n_M) = (20, 16)$ resulting in $t_{min}/r = 0.041$. Solution reported in (a) planar view, (b) perspective, and (c) principal cross-section.

along the meridians where the hoop forces are null, and a top cap is preserved uncracked. Numerically, this state can form since the height of the supports is encountered below the reference datum $z_b = -0.322$ m (see Fig. 9c). The forces in the structure vary from 0.0 kN to 83.5 kN.

For the maximum thrust solution (Fig. 10), a compressive ring is activated in the base of the dome, while the extreme points touching intrados and extrados are found in the same location. This suggests that under inward (active) displacement of the supports, a global mechanism for the dome is not activated, and the stability is ensured by the compressive ring in the base. The force value on this ring attains 107 kN. It is also noted that this ring creates a discontinuity on the thrust, as depicted in the section (Fig. 10c). Depending on the discretisation near the base, the force in the ring could attain infinity or be constrained by above by the parameter q_{max}. Such results are discussed in detail in [29].

5.2. Rounded cross vault

The second example refers to a rounded cross vault of variable thickness t on a square footprint with different springing angles β. The geometry of the rounded cross vault is obtained by intersecting two cylinders that have the same radius r. The square footprint has base length $l_0 = 10.0$ m, centre point at $(x_c, y_c, 0.0) = (5.0, 5.0, 0.0)$, and radius $r = 5.0$ m. To cope with the description as a function of β, the effective span s is introduced, computed as:

$$s = l_0 \cos(\beta), \tag{22}$$

which is used to compare the minimum thickness obtained for different springing angles β, with the adimensional t/s.

The three-dimensional geometry obtained for $\beta = 0°$, and $t_0 = 0.50$ m is depicted in Fig. 11a, and the effective span s consequence of the springing angle β is illustrated in Fig. 11b.

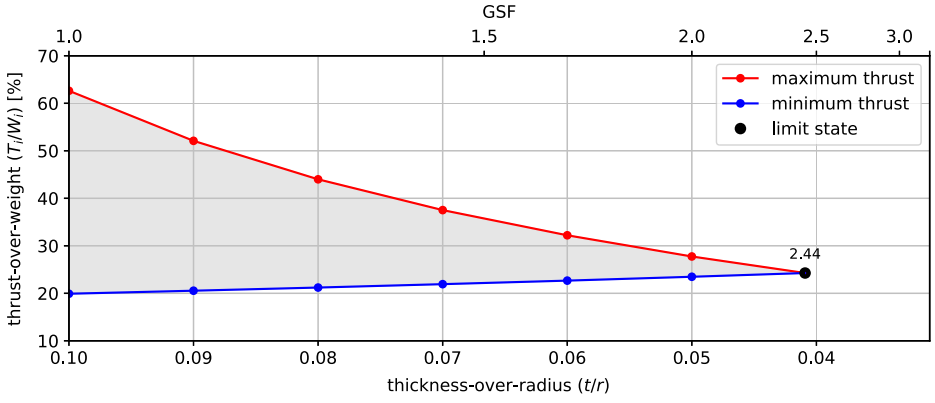

Fig. 8. Domain of stability obtained for the form diagram having discretisation $(n_P, n_M) = (20, 16)$. At the limit state, the GSF is plotted equals 2.44. (For interpretation of the references to color in this figure legend, the reader is referred to the web version of this article.).

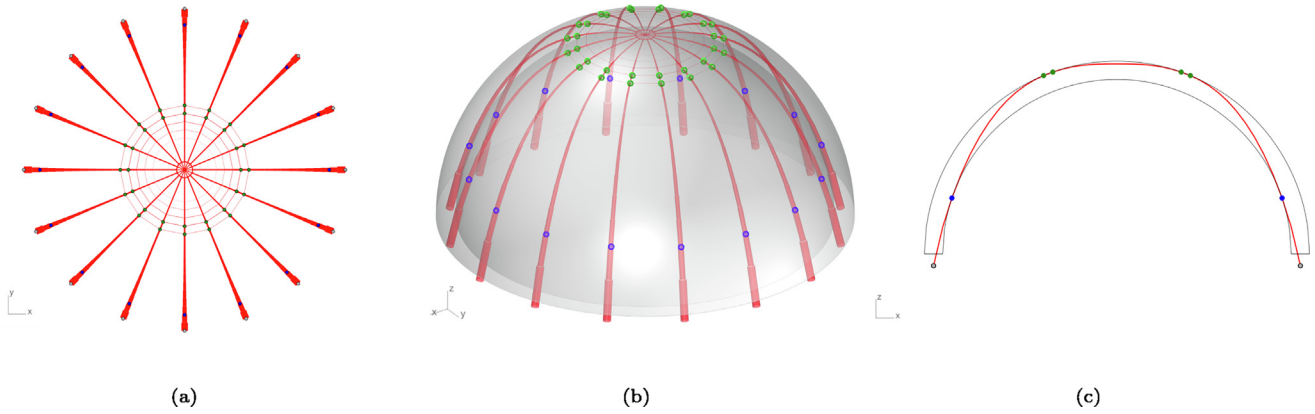

Fig. 9. Minimum thrust solution obtained for $(n_P, n_M) = (20, 16)$ and $t_0/r = 0.10$: (a) plan view (a), perspective (b), and principal cross-section.

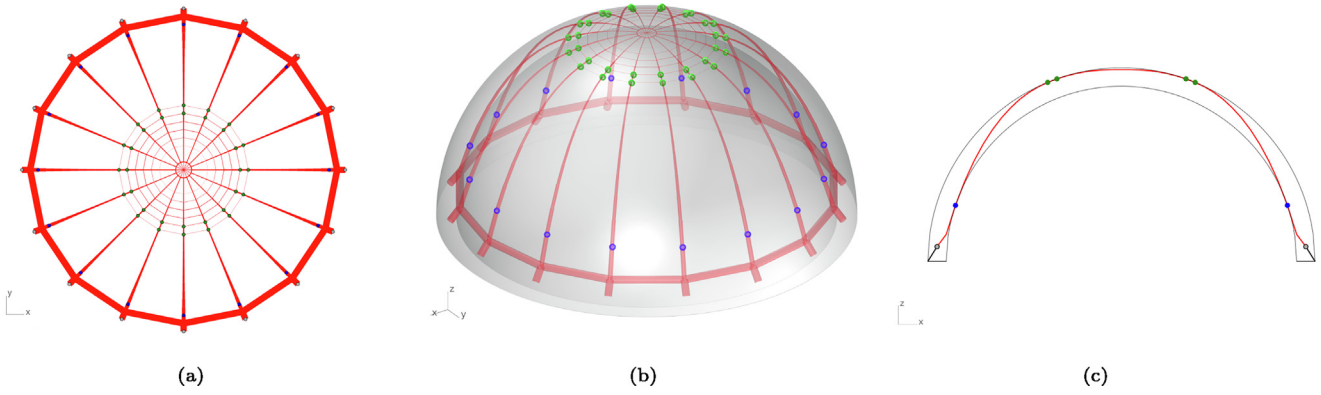

Fig. 10. Maximum thrust solution obtained for $(n_P, n_M) = (20, 16)$ and $t_0/r = 0.10$: (a) plan view (a), perspective (b), and principal cross-section.

For such parameters, the functions s_m, s_{LB} and s_{UB} representing middle, intrados, and extrados can be described for every point i present in the diagram with planar coordinates (x_i, y_i) as:

$$s_m(x_i, y_i, t) = \begin{cases} \sqrt{r^2 - (x_i - x_c)^2} & \text{if } (x_i, y_i) \in Q1, Q2 \\ \sqrt{r^2 - (y_i - y_c)^2} & \text{if } (x_i, y_i) \in Q3, Q4 \end{cases} \tag{23a}$$

$$s_{UB}(x_i, y_i, t) = \begin{cases} \sqrt{(r + t/2)^2 - (x_i - x_c)^2} & \text{if } (x_i, y_i) \in Q1, Q2 \\ \sqrt{(r + t/2)^2 - (y_i - y_c)^2} & \text{if } (x_i, y_i) \in Q3, Q4 \end{cases} \tag{23b}$$

$$s_{LB}(x_i, y_i, t) = \begin{cases} \sqrt{(r - t/2)^2 - (x_i - x_c)^2} & \text{if } (x_i, y_i) \in Q1, Q2 \text{ and } (x_i - x_c)^2 \leqslant (r - t/2)^2 \\ \sqrt{(r - t/2)^2 - (y_i - y_c)^2} & \text{if } (x_i, y_i) \in Q3, Q4 \text{ and } (y_i - y_c)^2 \leqslant (r - t/2)^2 \\ -z_{min} & \text{otherwise} \end{cases} \tag{23c}$$

where the quadrants Q1, Q2, Q3 and Q4 are depicted in Fig. 11a.

The weight density assumed is $\gamma = 20$ kN/m^3. The self-weight is applied considering the area of the middle surface of the cross vault and its thickness. For $t_0 = 0.50$ m and $\beta = 0°$ the self-weight is $W_0 = 1141$ kN.

5.2.1. Form diagrams considered

Unlike the well-known dome example, assuming a form diagram modelling the mechanical behaviour in the cross vault is not straight-forward [53]. In fact, the stability of cross vaults has been subject to multiple studies conducted with different modelling strategies, including discrete element [54], commercial finite element software [35], and lower-bound equilibrium methods [15]. In this section, we show how the proposed methodology represents a flexible and direct way to model the cross vault's structural response and to estimate its level of stability. Two different topologies are considered, as depicted in Fig. 12, named *orthogonal* and *fan-like* diagrams. Both form diagrams are parametrised according to the discretisation level defined by the number of subdivisions n varying in $n = (10, 12, 14, 16, 18, 20)$, resulting in six meshes for each topology. Only the four corners of each diagram are fixed. Fig. 12 highlights the two topologies and their independent edges for a level of discretisation defined by $n = 14$. In this case, the orthogonal diagram has 448 edges, of which 12 are independent, while the fan-like diagram has 784 edges, of which 30 are independent.

5.2.2. Analytical minimum thickness

A sensitivity analysis is carried out using the 12 diagrams studied, assuming $\beta = 0°$ and initial thickness $t_0 = 0.50$ m. The optimisation problem in Eqs. (15) of Section 4.2.1 is solved for each of these form diagrams. In this specific problem, the constraints on the outer limit of the extrados (Eqs. (15d) and (15e)) are disregarded, since cross vaults are often laterally supported by appropriate buttressing systems. The results of minimum thickness-over-span for the sensitivity analysis are depicted in Fig. 13.

Fig. 13 shows that the results of minimum thickness are highly sensitive to the topology of the form diagram. For $n = 20$, the minimum thickness-over-span obtained with the orthogonal diagram is $t_{min}/s = 0.033$, which represents a reduction of 30% when compared to the minimum thickness obtained with the fan-like

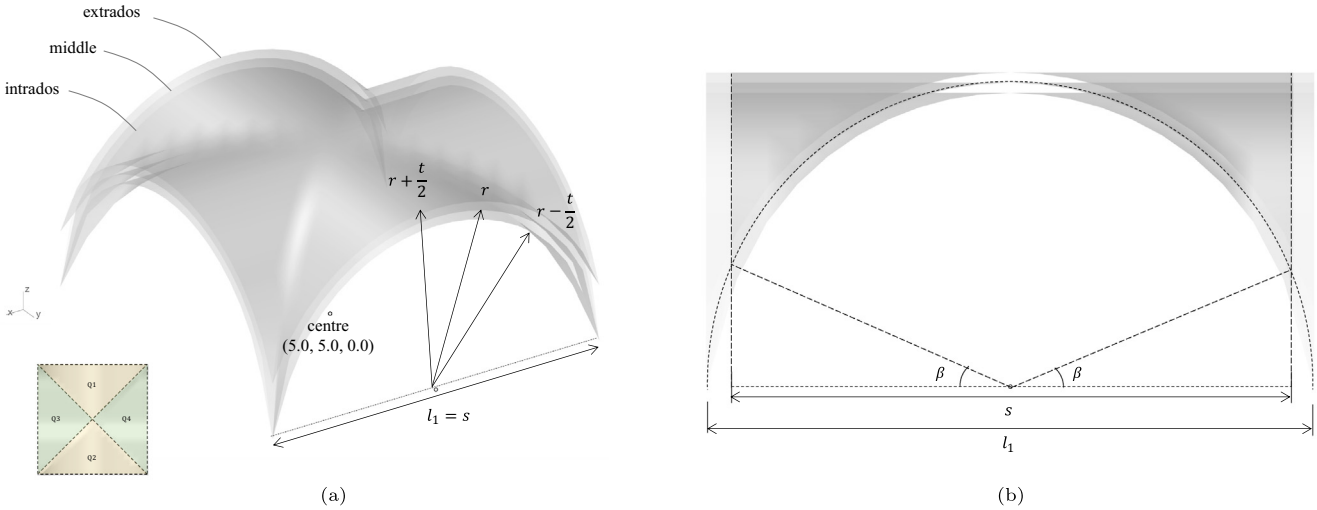

Fig. 11. (a) Three-dimensional geometry of the cross-vault with thickness $t = t_0 = 0.50$ m and $\beta = 0°$, and highlight on the quadrants Q1, Q2, Q3 and Q4 useful for the analytical description. (b) Springing angle β defining the effective span s.

diagram $t_{min}/s = 0.047$. Lower sensitivity is observed regarding the level of discretisation. Overall, for finer meshes (higher n), the minimum thickness-over-span increases slightly. Indeed, from the coarse $n = 10$ to the finer $n = 20$, an increase of about 10% is observed. These results show that the assumption on the flow of forces is crucial for the solution of the minimum thickness problem. The time consumption to solve the optimisation problems of this sensitivity study is presented in Table 2. The solving times vary from 0.4 to 9.8 s depending on the diagram topology and level of discretisation. Higher solving times are observed considering the fan-like topology, since this diagram has more independent edges.

The same optimisation is performed for different levels of springing angle $\beta = (0°, 5°, 10°, 15°, 20°, 25°, 30°, 35°, 40°)$ assuming $n = 14$. The results are depicted in Fig. 14:

As the springing angle increases, the minimum thickness decreases. The minimum thickness-over-span obtained with the orthogonal form diagram is as low as $t_{min}/s = 0.008$, for $\beta = 40°$. Similar trends are obtained for both diagrams, and the orthogonal diagram yields consistently smaller minimum thicknesses. In conclusion, the orthogonal diagram is better suited to the problem of rounded cross vaults. A further study on the minimum thickness of parametric cross vaults, considering different radius of curvature is presented in [55].

In the following subsection, this study is repeated considering the general procedure proposed in Section 4.2.2, which computes the minimum thickness without using the vault's analytical description.

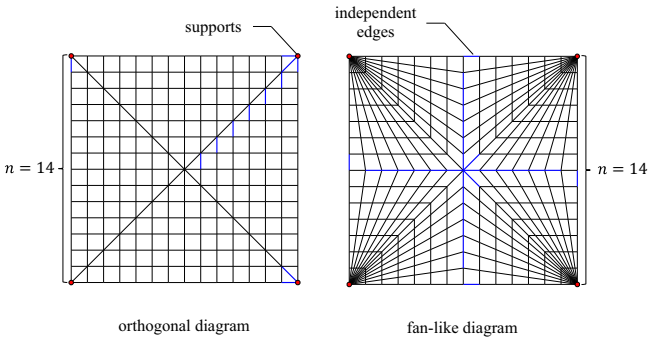

Fig. 12. Orthogonal (left) and fan-like (right) topologies considered for the diagrams with discretisation $n = 14$ and highlight in their independent edges (blue) and supports (red). (For interpretation of the references to color in this figure legend, the reader is referred to the web version of this article.)

5.2.3. General interpolation approach

Section 4.2.2 discusses a formulation to minimise the thickness of vaulted structures when the analytical description is unknown. The heights of the vault's geometry are extracted, and the general interpolation approach is executed assuming the two strategies A and B (Figs. 3a-b). Strategy A is based only on the information regarding the heights of the middle surface of the structure, while strategy B assumes that the heights of intrados and extrados are known. The results obtained with both strategies are compared with the results from the previous section. This comparison is presented in Figs. 15 and 16, for the orthogonal and fan-like form diagrams respectively.

The results show that the deviations observed with strategy A decrease with the increase in the springing angles, while strategy B results in good approximations of the analytical values for all ranges of β. For strategy A, higher deviations are present for low values of β due to the imprecision of the linear offset in the corners of the vault, where the geometry of intrados and extrados is almost vertical. Looking at the orthogonal

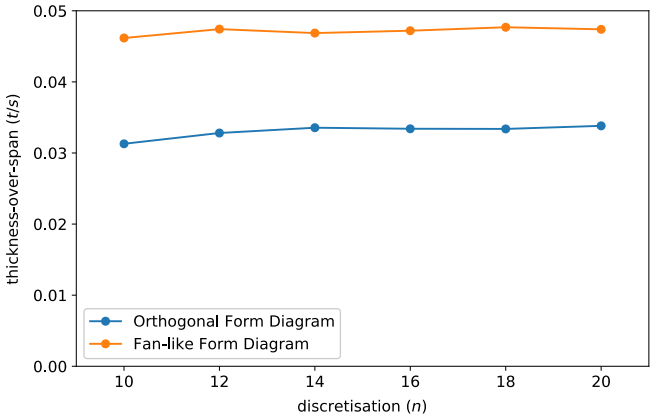

Fig. 13. Sensitivity analysis performed computing the minimum thickness-over-span assuming $\beta = 0°$. Results are grouped considering the two topologies (i.e., orthogonal and fan-like) in all discretisation levels.

Table 2
Solving times [sec] for the minimum thickness problem assuming different discretisation levels (n) with orthogonal and fan-like diagrams.

n	orthogonal	fan-like
10	0.4	0.7
12	0.6	1.4
14	0.6	2.7
16	1.3	2.9
18	1.5	5.5
20	2.5	9.8

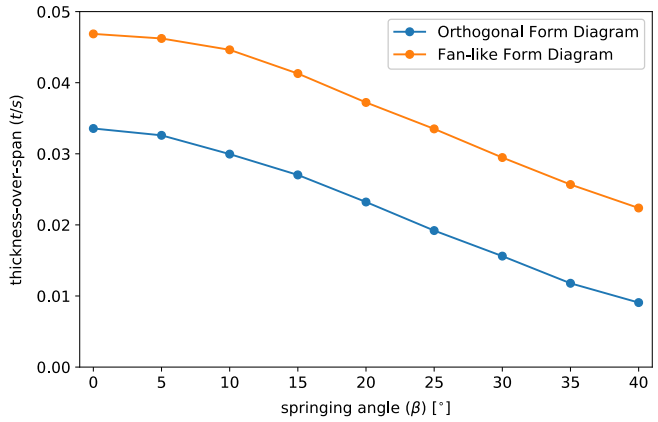

Fig. 14. Results of analytical minimum thickness obtained for orthogonal and fan-like diagrams considering different springing angles β, for a level of discretisation $n = 14$.

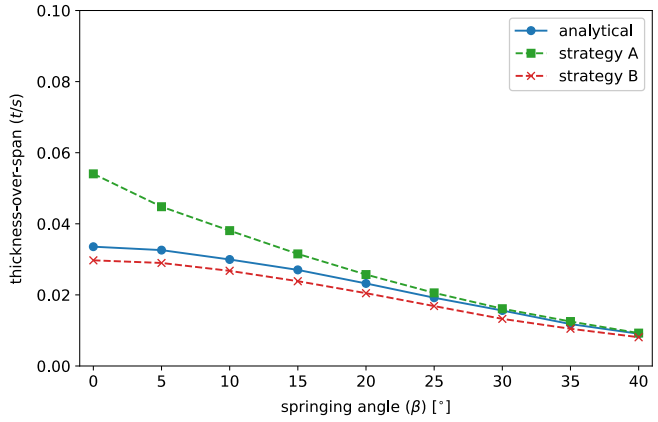

Fig. 15. Results of minimum thickness problem for the orthogonal diagram as function of the springing angle β and obtained with the analytical description using the two offset strategies: strategy A considers the bounds as an offset of the middle surface, and strategy B describes the reduced geometry as an offset of the initial intrados and extrados. Results are presented for a level of discretisation $n = 14$.

form diagram results (Fig. 15), the error at $\beta = 40°$ goes down to $+2\%$, and -11%, while with the fan-like form diagram results (Fig. 16), the error goes down to $+2\%$, and -5% for $\beta = 40°$, for the strategies A and B respectively. In practice, for $\beta = 40°$, the highest deviation observed shows an error lower than $t/s = 0.001$. Moreover, strategy A shows consistently conservative results, presenting a higher minimum thicknesses compared to the analytical methodology, while strategy B results in slightly under-conservative results.

In conclusion, these results encourage the application of the method as a suitable tool to analyse general masonry vaults that cannot be described analytically, particularly in the cases of non-zero springing angles, which are common in historic constructions.

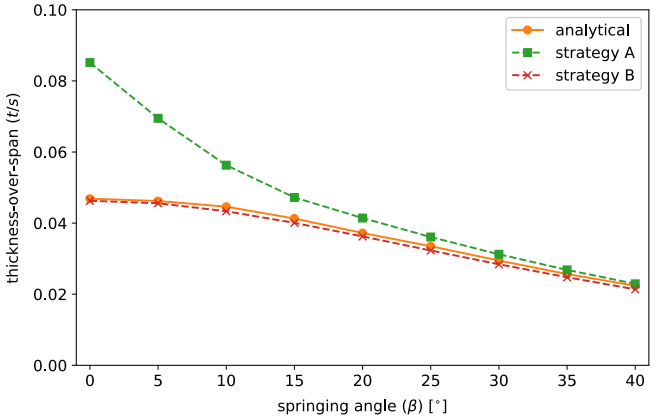

Fig. 16. Results of minimum thickness problem for the fan-like diagram as function of the springing angle β and obtained with the analytical description using the two offset strategies: strategy A considers the bounds as an offset of the middle surface, and strategy B describes the reduced geometry as an offset of the initial intrados and extrados. Results are presented for a level of discretisation $n = 14$.

5.2.4. Construction of the stability domain

The stability domain is computed for the two adopted form diagrams (orthogonal and fan-like) of the cross vault to measure the space of admissible solutions and to show the robustness of the vault for decreasing values of thickness. We consider three springing angles $\beta = (0°, 20°, 40°)$ and take the discretisation equals to $n = 14$ for both diagrams (Fig. 12). The results are depicted in Figs. 17 and 18.

The stability domain allows comparing the level of stability of the different structures. The larger the stability domain, the more stable the structure is. In both diagrams, it is clear that by increasing the springing angle β, the stability domain increases along with the corresponding GSF. Minimum and maximum thrust-overweight also tend to increase with the springing angle. The stability domain shrinks linearly towards the limit state, which gives an idea of the drop of the stability for reduced thicknesses. The stability domain for the orthogonal form diagram is always larger, reinforcing the conclusions of 5.2.2 that this diagram is better suited to the assessment analysis of rounded cross vaults.

The limit states obtained for $\beta = (0°, 20°, 40°)$ using the orthogonal and fan-like form diagrams are depicted in Figs. 19 and 20, respectively. In these figures, the touch-points at extrados (green) and intrados (blue) are highlighted. These touch-points suggest hinge lines with mechanisms appearing in the vault. The solutions in Figs. 19 and 20 show two hinge lines touching the extrados running parallel to the openings and crossing at the midspan of the vault. Additionally, touch-points in the intrados are observed in the vault's creases close to the supports.

5.3. Application to an existing geometry

To show how the proposed methodology can be applied to estimate the safety of cross vaults in a practical assessment scenario, the approximated geometry of the central nave at Amiens Cathedral [56,57] is considered. The idealised three-dimensional model is presented in Fig. 21a, from which the intrados and extrados of the vault are extracted. The geometry extracted corresponds to a rectangular pointed cross vault, with dimensions 6.0×11.2 m. The height from the impost line to the extrados is 4.75 m. The thickness extracted from the initial geometry is $t_0 = 0.44$ m. The point cloud depicted in Fig. 21b is retrieved from the idealised geometry and is used as the starting point to assess the stability of the vault. The point cloud is composed of 441 points for extrados and 441 points for intrados. Given that points

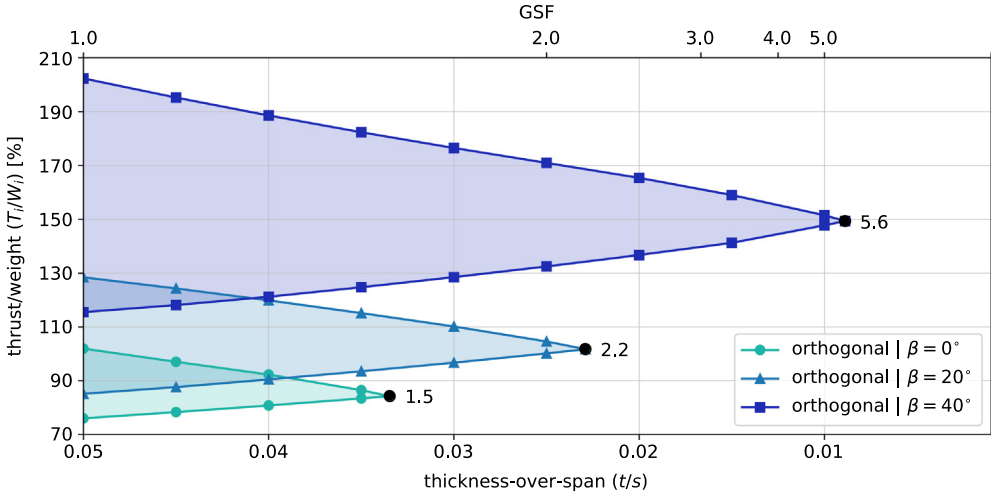

Fig. 17. Domain of Stability and Geometric Safety Factor obtained with orthogonal form diagram for initial thickness t_0, and three different springing angles $\beta = (0°, 20°, 40°)$ showing calculated GSF of 1.5, 2.2, and 5.6, respectively. The area for each β between maximum and minimum thrust for different thickness is highlighted and corresponds to the domain of admissible stress state computed.

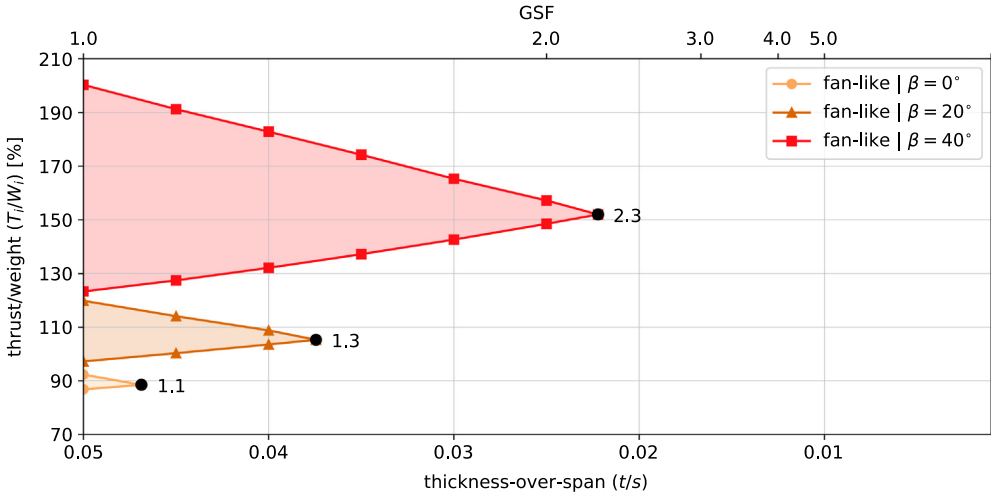

Fig. 18. Domain of Stability and Geometric Safety Factor obtained with fan-like form diagram for initial thickness t_0, and three different springing angles $\beta = (0°, 20°, 40°)$ showing calculated GSF of 1.1, 1.3, and 2.3, respectively. The area for each β between maximum and minimum thrust for different thickness is highlighted and corresponds to the domain of admissible stress state computed.

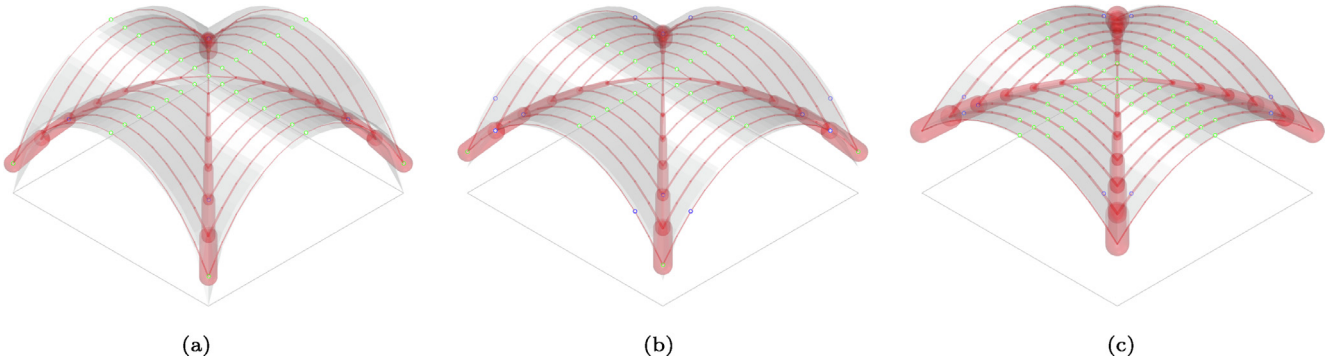

Fig. 19. Solution of minimum thickness obtained with different β assuming the orthogonal form diagram. For (a) β=0°, $t_{min}/s = 0.033$; for (b) β=20°, $t_{min}/s = 0.023$; and (c) for β=40°, $t_{min}/s = 0.009$. Figures are shown with the same effective span s.

representing the intrados and the extrados are available, strategy B considering the information about these two surfaces is adopted (Section 4.2.2b) to this case study. This strategy consists of minimising the thickness of the structure by maximising the parameter α (Eqs. (19)) that represents the offset distance applied to intrados and extrados.

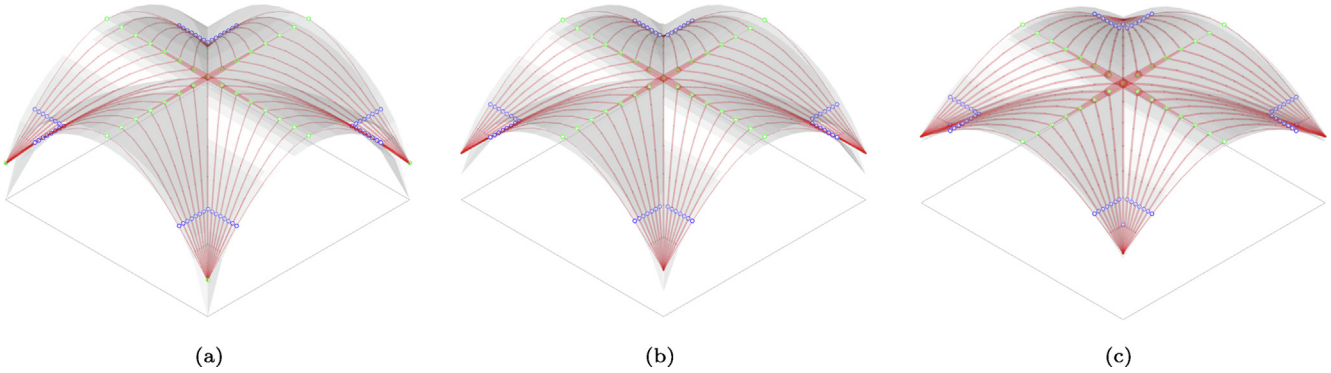

Fig. 20. Solution of minimum thickness obtained with different β assuming the fan-like form diagram. For (a) β=0°, $t_{min}/s = 0.047$; for (b) β=20°, $t_{min}/s = 0.037$; and (c) for β=40°, $t_{min}/s = 0.022$. Figures are shown with same effective span s.

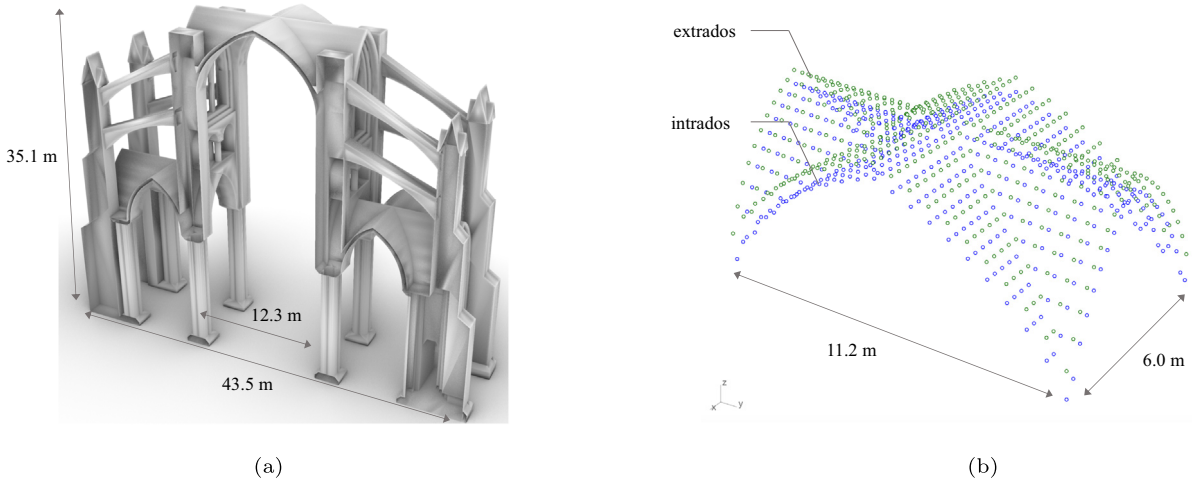

Fig. 21. (a) Approximate geometry of Amiens Cathedral assumed. (b) Point cloud extracted to execute the analysis: green points representing extrados and blue representing the intrados. (For interpretation of the references to color in this figure legend, the reader is referred to the web version of this article.).

5.3.1. Form diagrams considered

The topologies from Fig. 22 are adopted, with the diagrams stretched to match the rectangular footprint of the vault $(l_x, l_y) = (6.0, 11.2)$. The diagrams assume a level of discretisation $n = 14$.

5.3.2. Minimum thickness and stability domain

The minimum thickness is calculated for both diagrams, and the results obtained show $\alpha_{max} = -0.16$ and $\alpha_{max} = 0.09$ for orthogonal and fan-like diagrams, respectively. Since the result for the orthogonal diagram is negative, this topology is not suitable for the assessment of this problem, because it would result in a minimum thickness superior to the actual thickness of the vault. Using the fan-like form diagram, the minimum thickness is calculated as $t_{min} = 0.44 - 2 * \alpha_{max} = 0.281$ m, which results in a GSF equals to 1.56.

The stability domain is also traced for this pointed cross vault. The results of minimum and maximum thrust for different values of thicknesses (computed from different levels of offset α) are depicted in Fig. 23. This diagram allows extracting maximum and minimum thrust-over-weight ratios, which in this case are equal to $T_{max}/W = 85\%$ and $T_{min}/W = 70\%$. In addition, as the thickness decreases towards the limit state, the stability domain shrinks linearly until the thickness of 0.32 m, after which the difference among minimum and maximum thrusts drops sharply.

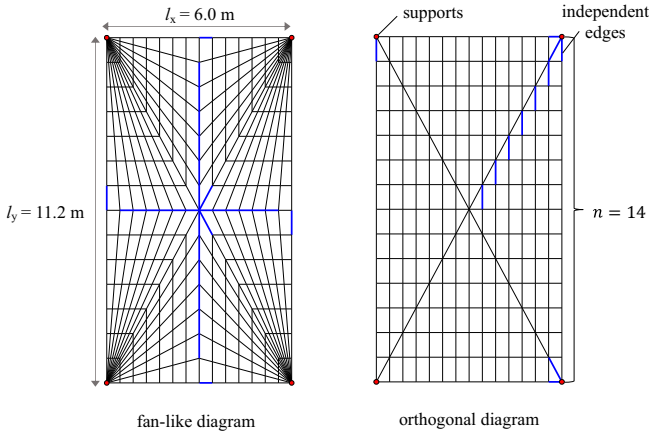

Fig. 22. Rectangular diagrams (fan-like and orthogonal) used in the analysis of the vault at Amiens Cathedral with highlight on the supports (red) and independent edges (blue) of each topology. (For interpretation of the references to color in this figure legend, the reader is referred to the web version of this article.)

In conclusion, unlike the application on rounded cross vaults, the fan-like form diagram is a more suitable force flow for the pointed cross vault application of this section, as evidenced by

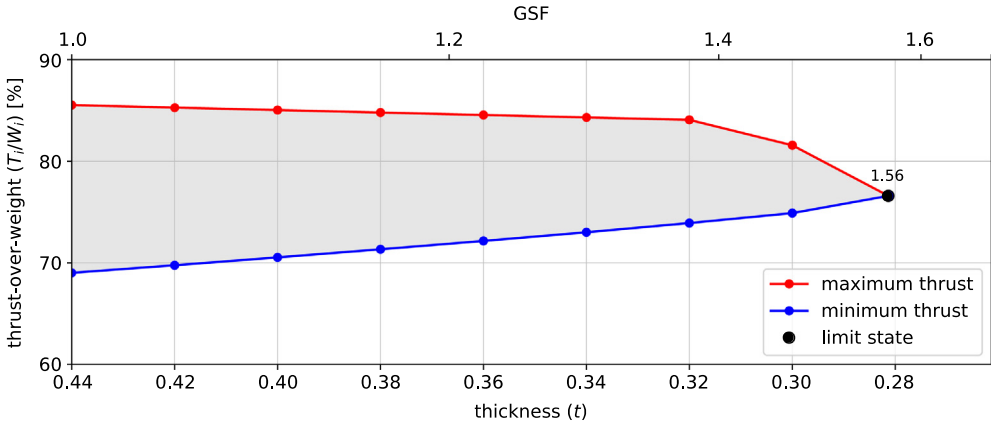

Fig. 23. Minimum thrust solution obtained for the discretisation $n = 14$ and initial thickness $t_0 = 0.44$ m considering the fan-like form diagram.

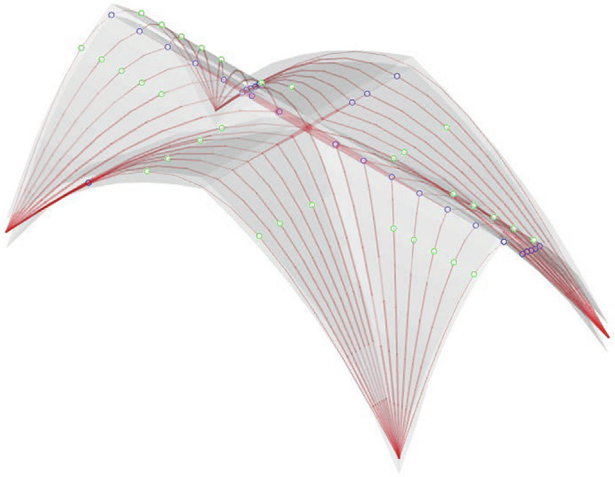

Fig. 24. Thrust network obtained for the minimum thickness of the pointed cross vault representing the vaults of Amiens Cathedral. The minimum thickness is obtained with the fan-like form diagram, calculated as $t_{min} = 0.281$ m, which results in a GSF = 1.56 for the problem.

the smaller limit thickness, which indicates that the forces on the proposed geometry flow to the supports without accumulating on the diagonals, or creases of the vault. In Fig. 24, the thrust network obtained at the minimum thickness optimisation is presented, highlighting the points where it touches intrados and extrados. Due to the scattered input data, the solution obtained in this numerical simulation is not perfectly symmetrical. Additionally, since the computation of such diagrams, including all the optimisation problems for minimum and maximum thrusts, takes less than a minute, different force flows could be confronted in practical assessment scenarios, searching for higher GSF, and reducing the dependency on the network topology.

6. Conclusions

This paper introduces a new methodology to quantify the stability of vaulted masonry structures using Thrust Network Analysis. Networks with fixed horizontal projection are considered with their stress states described as a function of the force densities of the independent edges. The proposed approach formulates and solves constrained nonlinear optimisation problems (NLP) with specific objective functions. The method yields two assessment outputs: the Geometric Safety Factor (GSF) and the stability domain. The GSF is obtained by solving a direct NLP which has the minimisation of the structural thickness as its objective. This minimisation considers a proper orthogonal reduction of the thickness, which can be applied to analytically and numerically described geometries. The stability domain is obtained by setting the NLP objective to minimise and maximise the (horizontal) thrust for decreasing structural thicknesses, resulting in a diagram that gives a consistent measurement of the size of the space of admissible stress states and of the robustness of the structure.

The numerical strategy is implemented within the Python-based COMPAS open-source framework [32], specifically within the COMPAS Masonry project [58], where different masonry analysis tools are also available. The effectiveness of the present methodology is demonstrated in a series of case studies considering vaulted structures of increasing complexity.

Firstly, the values of GSF for a hemispherical dome are obtained and compared with the literature showing small deviations of around 2%. A sensitivity study is performed to the discretisation level of the networks, identifying the discretisation required to observe the convergence of the values of minimum thickness. The stability domain is also obtained for the dome showing how the level of stability drops towards the limit state.

Secondly, the GSF of parametric rounded cross vaults with different springing angles is calculated. Then, the results with the analytical description of the geometries are compared to the results obtained considering approximated meshes. The error by considering approximated surfaces is low (down to 2%), especially if realistic springing angles (i.e., greater than 20°) are considered. The stability domain is obtained for cross vaults with different springing angles and as a function of different form diagrams. It shows how varying the form diagrams is important to performing a proper assessment of cross vaults.

Finally, an approximated cross vault geometry of Amiens Cathedral described by point clouds is analysed. With this input, the GSF and the stability domain are obtained, reflecting the flexibility of the present methodology.

Regarding the numerical implementation, the NLPs formulated consider analytic expressions for the sensitivities and are solved in a few seconds. A preconditioning step is necessary to select the independent edges in the form diagram, which is executed with an improved and fast interactive algorithm.

The main drawback of the method is the dependency of the results on the assumption of the form diagram. After its selection, the diagram remains fixed throughout the analysis. However, as the solutions are always a lower bound of both the collapse state and the GSF, different form diagrams are used on the same geometry to look for larger GSFs and, thus, wider stability domains. Nevertheless, future work will focus on adaptation strategies for the form diagrams and further detailed investigations of their

corresponding stability domains, as well as comparing the present approach to others, such as rigid block equilibrium, discrete element modelling, and finite element modelling.

Funding

This work was supported by the SNSF - Swiss National Science Foundation. Project grant n. 178953: "Practical Stability Assessment Strategies for Vaulted Unreinforced Masonry Structures".

Declaration of Competing Interest

The authors declare that they have no known competing financial interests or personal relationships that could have appeared to influence the work reported in this paper.

References

[1] Tralli A, Alessandri C, Milani G. Computational methods for masonry vaults: A review of recent results. Open Civ Eng J 2014;8(1).
[2] Huerta S. Mechanics of masonry vaults: the equilibrium approach. In: Lourenço P, Roca P, editors. Historical Constructions. Possibilities of numerical and experimental techniques, vol. 1. Guimarães: Universidade do Minho; 2001. p. 47–70.
[3] Huerta S. The analysis of masonry architecture: A historical approach. Architec Sci Rev 2008;51(4):297–328.
[4] Heyman J. The stone skeleton. Int J Solids Struct 1966;2(2):249–79.
[5] Ochsendorf J. Collapse of masonry structures [PhD thesis]. Cambridge: University of Cambridge; 2002.
[6] Poleni G. Memorie Istoriche della gran cupola del tempio vaticano. Padova: Nella Stamperia del Seminario 1748..
[7] Wolfe WS. Graphical Analysis: A Text Book on Graphic Statics. New York: McGraw-Hill Book Co., Inc.; 1921.
[8] Zessin J, Lau W, Ochsendorf J. Equilibrium of cracked masonry domes. Proc Inst Civ Eng Eng Comput Mech 2010;163(3):135–45.
[9] Nodargi N, Bisegna P. A new computational framework for the minimum thrust analysis of axisymmetric masonry domes. Eng Struct 2021;234:111962.
[10] Angelillo M, Olivieri C, DeJong MJ. A new equilibrium solution for masonry spiral stairs. Eng Struct 2021;238(April):112176.
[11] Fraternali F, Angelillo M, Fortunato A. A lumped stress method for plane elastic problems and the discrete-continuum approximation. Int J Solids Struct 2002;39(25):6211–40.
[12] Fraternali F. A thrust network approach to the equilibrium problem of unreinforced masonry vaults via polyhedral stress functions. Mech Res Commun 2010;37(2):198–204.
[13] Angelillo M, Babilio E, Fortunato A. Singular stress fields for masonry-like vaults. Continuum Mech Thermodyn 2013;25(2–4):423–41.
[14] Fraddosio A, Lepore N, Piccioni MD. Thrust Surface Method: An innovative approach for the three-dimensional lower bound Limit Analysis of masonry vaults. Eng Struct 2020;202:109846.
[15] Montanino A, Olivieri C, Zuccaro G, Angelillo M. From stress to shape: Equilibrium of cloister and cross vaults. Appl Sci 2021;11(9).
[16] Miki M, Igarashi T, Block P. Parametric self-supporting surfaces via direct computation of airy stress functions. ACM Trans Graph SIGGRAPH 2015;34(4). 89:1–11.
[17] Vouga E, Höbinger M, Wallner J, Pottmann H. Design of self-supporting surfaces. ACM Trans Graph 2012.
[18] de Goes F, Alliez P, Owhadi H, Desbrun M. On the equilibrium of simplicial masonry structures. ACM Trans Graph July 2013;32.
[19] Block P, Ochsendorf J. Thrust network analysis: A new methodology for three-dimensional equilibrium. J Int Assoc Shell Spatial Struct December 2007;48:167–73.
[20] Block P. Thrust Network Analysis: Exploring Three-dimensional Equilibrium [PhD thesis]. Cambridge, MA, USA: Massachusetts Institute of Technology; 2009.
[21] Marmo F, Rosati L. Reformulation and extension of the thrust network analysis. Comput Struct 2017;182:104–18.
[22] Van Mele T, Panozzo D, Sorkine-Hornung O, Block P. Best-fit thrust network analysis - rationalization of freeform meshes. In: Adriaenssens S, Block P, Veenendaal D, Williams C, editors. Shell Structures for Architecture: Form Finding and Optimization. London: Routledge; 2014.
[23] Block P, Lachauer L. Three-dimensional funicular analysis of masonry vaults. Mech Res Commun 2014;56:53–60.
[24] Bruggi M. A constrained force density method for the funicular analysis and design of arches, domes and vaults. Int J Solids Struct 2020;193–194:251–69.
[25] Heyman J. The Stone Skeleton: Structural Engineering of Masonry Architecture. Cambridge University Press; 1995.
[26] Fraddosio A, Lepore N, Piccioni MD. Thrust Surface Method: An innovative approach for the three-dimensional lower bound Limit Analysis of masonry vaults. Eng Struct Jan 2020;202:109846.
[27] O'Dwyer D. Funicular analysis of masonry vaults. Comput Struct 1999;73(1–5):187–97.
[28] Marmo F, Masi D, Mase D, Rosati L. Thrust network analysis of masonry vaults. Int J Masonry Res Innov 2019;4(1–2):64–77.
[29] Maia Avelino R, Iannuzzo A, Van Mele T, Block P. New strategies to assess the safety of unreinforced masonry structures using thrust network analysis. In: Proceedings of the SAHC Symposium 2021, (Barcelona, Spain); 2021.
[30] Romano A, Ochsendorf JA. The mechanics of gothic masonry arches. Int J Architec Heritage 2010;4(1):59–82.
[31] Block P, Ciblac T, Ochsendorf J. Real-time limit analysis of vaulted masonry buildings. Comput Struct 2006;84(29):1841–52.
[32] Van Mele T. COMPAS: A framework for computational research in architecture and structures; 2017–2021. http://compas.dev/.
[33] Kraft D. A software package for sequential quadratic programming. Tech. Rep. DFVLR-FB 88-28. Koln, Germany: German Aerospace Center – Institute for Flight Mechanics; 1988.
[34] Prager W. An Introduction to Plasticity. Addison-Wesley series in the engineering sciences. Addison-Wesley Publishing Company; 1959.
[35] Milani G, Milani E, Tralli A. Upper bound limit analysis model for FRP–reinforced masonry curved structures. part ii: Structural analyses. Comput Struct 2009;87(23):1534–58.
[36] Milani G, Tralli A. A simple meso-macro model based on SQP for the non-linear analysis of masonry double curvature structures. Int J Solids Struct 2012;49(5):808–34.
[37] Chiozzi A, Milani G, Tralli A. A genetic algorithm NURBS-based new approach for fast kinematic limit analysis of masonry vaults. Comput Struct 2017;182:187–204.
[38] Grillanda N, Chiozzi A, Milani G, Tralli A. Collapse behavior of masonry domes under seismic loads: An adaptive NURBS kinematic limit analysis approach. Eng Struct 2019;200:109517.
[39] Bagi K. When heyman's safe theorem of rigid block systems fails: Non-heymanian collapse modes of masonry structures. Int J Solids Struct 2014;51(14):2696–705.
[40] Beatini V, Royer-Carfagni G, Tasora A. Modeling the shear failure of segmental arches. Int J Solids Struct 2019;158:21–39.
[41] Baratta A, Corbi O. The Static Behavior of Historical Vaults and Cupolas. In: Jasieńko J, editor. Structural Analysis of Historical Constructions. Poland): Wroclaw; 2012.
[42] Beatini V, Royer-Carfagni G, Tasora A. The role of frictional contact of constituent blocks on the stability of masonry domes. Proc Roy Soc Math Phys Eng Sci Jan 2018;474:20170740.
[43] Chen S, Bagi K. Crosswise tensile resistance of masonry patterns due to contact friction. Proc Roy Soc Math Phys Eng Sci Aug 2020;476:20200439.
[44] Schek H-J. The force density method for form finding and computation of general networks. Comput Methods Appl Mech Eng 1974;3(1):115–34.
[45] Van Mele T, Block P. Algebraic graph statics. CAD Comput Aided Des 2014;53:104–16.
[46] Pellegrino S, Calladine CR. Matrix analysis of statically and kinematically indeterminate frameworks. Int J Solids Struct 1986;22(4):409–28.
[47] Liew A, Avelino R, Moosavi V, Van Mele T, Block P. Optimising the load path of compression-only thrust networks through independent sets. Struct Multidiscipl Optimiz 2019;60:231–44.
[48] Fantin M. Étude des rapports entre stéréotomie et résistance des voûtes clavées. Theses: Université Paris-Est; 2017.
[49] Chen X, Lin Q. Properties of Generalized Offset Curves and Surfaces. J Appl Math 2014;2014:124240.
[50] Ross E, Hambleton D. Exact face-offsetting for polygonal meshes. In: Combs L, Perry C, editors. Computational ecologies: design in the anthropocene Proceedings of the 35th Annual Conference of the Association for Computer Aided Design in Architecture (ACADIA), vol. 1. Cincinnati: CUMINCAD; 2015. p. 203–9.
[51] Jones E, Oliphant T, Peterson P. SciPy: open source scientific tools for Python; 2001.
[52] Liew A, Pagonakis D, Van Mele T, Block P. Load-path optimisation of funicular networks. Meccanica 2018;53:279–94.
[53] Block P, Lachauer L. Three-dimensional equilibrium analysis of gothic masonry vaults. Int J Architec Heritage 2014;8(3):312–35.
[54] Van Mele T, McInerney J, DeJong M, Block P. Physical and computational discrete modeling of masonry vault collapse. In: Proceedings of the 8th International Conference on Structural Analysis of Historical Constructions (Wroclaw, Poland).
[55] Maia Avelino R, Iannuzzo A, Van Mele T, Block P. Parametric stability analysis of groin vaults. Appl Sci 2021;11(8).
[56] Viollet-le Duc EE. Dictionnaire raisonné de l'architecture française du XIe au XVIe siècle, vol. 1. Banc; 1854.
[57] Coccia S, Como M, Di Carlo F. Wind strength of gothic cathedrals. Eng Fail Anal 2015;55:1–25.
[58] Iannuzzo A, Dell'Endice A, Maia Avelino R, Kao G, Van Mele T, Block P. Compas masonry: A computational framework for practical assessment of unreinforced masonry structures. In: Proceedings of the SAHC Symposium 2021, (Barcelona, Spain); 2021.